



Probabilistic tsunami hazard assessment at Stromboli volcano: 2. New simulation database and probabilistic inundation maps and curves

Mattia de' Michieli Vitturi¹, Alessandro Tadini¹, Andrea Bevilacqua¹, Juan F. Rodríguez-Gálvez^{1,2}, Matteo Cerminara¹, Tomaso Esposti Ongaro¹, Augusto Neri¹, Matteo Trolese¹, Jorge Macías², Manuel J. Castro², Cipriano Escalante², Sergio Ortega², José M. González-Vida², Stefano Lorito³

¹Istituto Nazionale di Geofisica e Vulcanologia, Sezione di Pisa, via Cesare Battisti 53, 56125 Pisa, Italy.

²EDANYA Group, Universidad de Málaga, Avda. Cervantes 2, 29071 Málaga, Spain

³Istituto Nazionale di Geofisica e Vulcanologia, Sezione ONT, Via di Vigna Murata 605, 00143 Roma, Italy

Correspondence to: Mattia de' Michieli Vitturi (mattia.demichielivitturi@ingv.it), Alessandro Tadini (alessandro.tadini@ingv.it)

Abstract. Probabilistic Tsunami Hazard Assessment (PTHA) is the essential first step for quantifying the long-term risk posed by landslide-generated tsunamis at active volcanic islands like Stromboli, Italy. This study presents a first PTHA for Stromboli, providing a quantitative and transparent basis for risk mitigation and long-term coastal planning at Stromboli. In particular, our work integrates two new databases of numerical simulations for volcanic landslide-induced tsunamis with occurrence probabilities derived from expert elicitation (described in the companion paper by Tadini et al., submitted). We introduce a new methodology to translate elicited probabilities for landslide frequency, volume, and location into a full suite of probabilistic hazard products. The results, expressed as hazard curves, maps and profiles (5th, 50th and 95th percentiles), are presented for alternative modelling setups, including different high-resolution topobathymetric models and code versions, to transparently account for epistemic uncertainty in the numerical hazard assessment. Our findings quantify a significant tsunami hazard for Stromboli's inhabited coastal areas over the next 50 years. The 95th percentile maps indicate that inundation by at least 0.5 m of water has > 90% to occur along coast of Stromboli village the over the next 50 years. Furthermore, the hazard curves at critical sites show non-negligible probabilities of exceeding severe inundation depths in the same 50 years temporal frame.

1 Introduction

Probabilistic Tsunami Hazard Assessment (PTHA) has become the standard framework for quantifying tsunami hazard, moving beyond deterministic, single-scenario analyses to provide a more comprehensive understanding of risk (Grezio et al., 2017; Selva et al., 2021). PTHA aims to estimate the probability of exceeding specific tsunami intensity metrics (such as inundation depth) at a given location, or conversely, to estimate the intensity metric corresponding to a given probability of



exceedance, over a defined time horizon. This approach allows for the systematic integration of multiple tsunami sources and the quantification of both aleatory and epistemic uncertainties (Lorito et al., 2021), providing a robust basis for risk mitigation and coastal planning (Behrens et al., 2021).

35 Among the various tsunamigenic sources, landslides from volcanic islands represent a significant but complex challenge for PTHA due to the inherent instability of volcanic edifices. At Stromboli volcano (Aeolian Islands, Italy), the persistent, centuries-long volcanic activity (e.g., Barberi et al., 1993; Rosi et al., 2013; Tadini et al., submitted) feeds the Sciara del Fuoco (SdF), a large horseshoe-shaped scar on the volcano's northwestern flank that is prone to both subaerial and submarine failures. The tsunamigenic potential of the SdF was dramatically demonstrated on December 30, 2002, when a sequence of landslides triggered a tsunami that caused significant damage to the island's coastline (Tinti et al., 2006b).

40 The 2002 event spurred significant research into the numerical modelling of landslide-generated tsunamis at Stromboli. Tinti et al. (2000, 2005, 2006b) and Fornaciai et al. (2019, 2024) presented numerical simulation results to investigate the 2002 event. Subsequent work by Esposti Ongaro et al. (2021; 2025) advanced these efforts through a systematic benchmark of different numerical codes and physical approximations. These studies highlighted the critical importance of using non-hydrostatic models to accurately capture wave generation and propagation in the near-field and explored the differences
45 between rigid and deformable (granular) landslide models.

Beyond its scientific relevance, the 2002 event also forms the basis of the current civil protection plan in Stromboli (Protezione Civile, 2015). However, the new Italian Civil Protection Code explicitly promotes the use of probabilistic approaches, whenever possible, to assess potential risks (Protezione Civile, 2018a). In line with this, emergency planning for earthquake-generated tsunamis in Italy (Protezione Civile, 2018b) is already based on a regional long-term PTHA model (Basili et al.,
50 2021; Tonini et al., 2021). Furthermore, for early-warning purposes related to earthquake-generated tsunamis, Italy has adopted Probabilistic Tsunami Forecasting (Selva et al., 2021; Cordrie et al., 2025), which can be regarded as a very short-term PTHA. In this context, the present paper is the second of two companion articles reporting the results of a comprehensive project aimed at developing the first formal long-term PTHA for volcanic landslide-generated tsunamis at Stromboli.

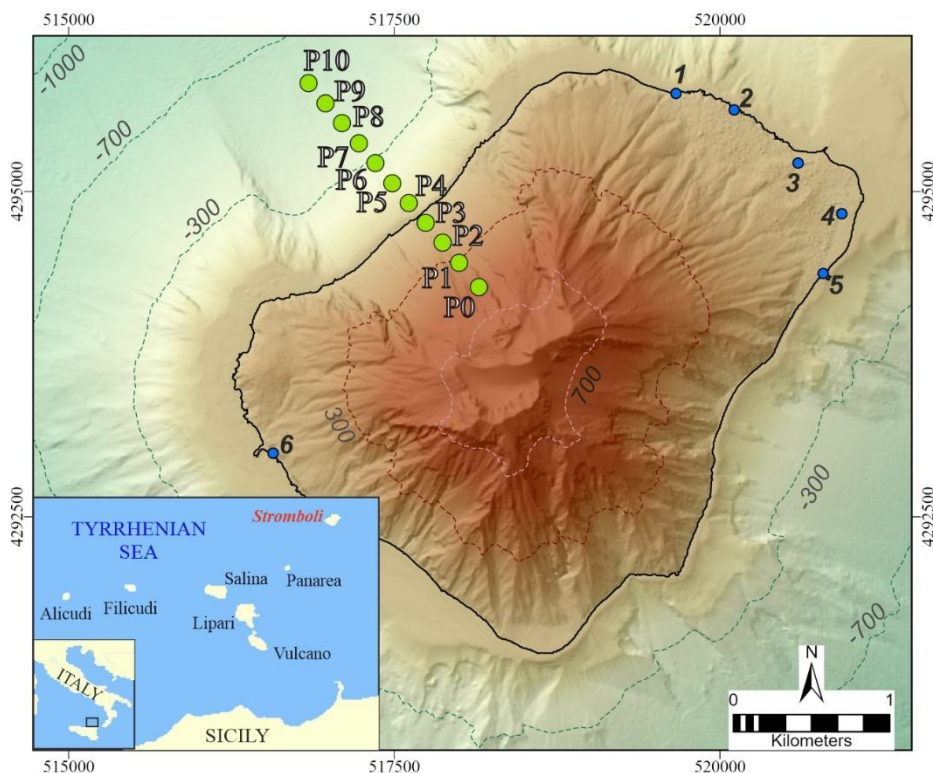
55 Developing a comprehensive PTHA that incorporates a temporal framework requires establishing a historical baseline of tsunami occurrences in a specific area to derive future occurrence rates. However, although Stromboli allows for a detailed review of historical sources, the available data are still insufficient for a robust statistical analysis. To address this, expert elicitation techniques (see e.g., Aspinall, 2006; Colson and Cooke, 2018; Quigley et al., 2018) represent an established approach in volcanology to quantify uncertainties in key variables (such as occurrence rates and magnitudes) in contexts where a lack of observational constraints and/or inadequate data prevent traditional analysis.

60 The companion paper by Tadini et al. (submitted) provides a detailed review of historical tsunami events at the island and, crucially, presents the results of a structured expert elicitation. That elicitation was designed to formally quantify the epistemic uncertainties associated with the key source parameters for tsunami modelling, providing probability distributions for the frequency, location, and volume of future tsunamigenic landslides (TLs) at the SdF (Fig. 1).



65 Building on that work, this paper utilizes the probabilistic outputs of the expert elicitation to probabilistically weight the scenarios contained in two new databases of numerical tsunami simulations (de' Michieli Vitturi et al., 2026a-b). We present a new methodology to integrate the probability distributions from the elicitation with the scenarios of the simulation databases to obtain a PTHA. The final products of this work are the first hazard curves at several points and probabilistic inundation maps for Stromboli (Fig. 1), expressing the probability of exceeding a given tsunami intensity value in the next 50 years, which account for the full range of elicited uncertainty. A key aspect of this study is the exploration of epistemic uncertainty
70 introduced by numerical modelling. Accounting for land cover roughness is particularly critical, as it has been shown to significantly affect inundation extent (see e.g., Dalrymple et al., 2006; Kaiser et al., 2011; Griffin et al., 2015; Scala et al., 2024). In this work, we quantify epistemic uncertainty associated with the modelling by presenting results for two different high-resolution topographic models (20 m and 10 m) and two versions of the same numerical code.

This paper is organized as follows. Section 2 describes the numerical models, the simulation databases, and the strategy
75 developed to integrate the expert elicitation outcomes for the generation of probabilistic curves and maps. Section 3 presents the main results, including a comparison of the hazard products derived from the different model setups and a detailed analysis of the hazard patterns. Finally, Section 4 provides some discussion and Section 5 summarizes the main conclusions of this study.



80 **Figure 1.** Stromboli volcano. Initial positions for simulations along the Sciara del Fuoco (see Section 2.2) are indicated as green points. Sites where hazard curves have been described (see Section 2.3.1) are indicated as blue points (1: Spiaggia Lunga; 2: Scalo dei Balordi; 3: Area attesa Ficogrande; 4: Centrale ENEL; 5: Molo Scari; 6: Molo Ginostra). The solid black line is the coastline. Hillshade relief is derived from a resampling at 10-m resolution of, respectively, the DSM of Bisson et al. (2025) for the subaerial part, and the bathymetry provided by I.I.M.M. (Istituto Idrografico Marina Militare - Italian Navy
85 Hydrographic Institute) for the submarine part. Coordinates are expressed in the UTM-WGS84 33 N system.

2 Materials and Methods

2.1 Expert elicitation

Performance-based expert elicitation relies on empirical validation using quantitative calibration questions, or "seed questions", whose true answers are known to analysts but not to experts (Colson and Cooke, 2018; Quigley et al., 2018).
90 Experts also address "target questions" on the key issues of the problem under investigation. For both types, they provide 5th, 50th, and 95th percentiles of their uncertainty. A performance-based algorithm then combines expert opinions into group-level uncertainty distributions (Decision Maker solutions) using either equal weighting (EW) or Cooke's Classical Model (CM) (Cooke, 1991; Aspinall, 2006, 2010; Neri et al., 2008; Bevilacqua, 2016). CM weights experts based on calibration (statistical



accuracy) and informativeness, computed from seed question responses (Cooke, 1991; Aspinall and Cooke, 2013; Bevilacqua
 95 et al., 2015, 2025; Tadini et al., 2017, 2022). The web-based tool ELICIPY (de' Michieli Vitturi et al., 2024) was used to
 manage elicitation sessions, from data collection to automated analysis and output generation.

The elicitation was aimed at estimating, for the next 50 years: i) the expected number of TLs with volumes $\geq 1 \times 10^6 \text{ m}^3$ at
 Stromboli, and ii) their potential triggering conditions and parameters. Two expert elicitations were conducted (in 2022 and
 2024), the second of which was designed to resolve ambiguities in some initial questions and to incorporate new field data that
 100 had become available. In total, 21 experts with diverse expertise and strong knowledge of Stromboli participated. Seed
 questions (16 total) were included only in the first round. Target questions focused on landslides $\geq 1 \times 10^6 \text{ m}^3$ - roughly half
 the subaerial mass deposited during June – October 2019 (Di Traglia et al., 2022) and 20–30 times smaller than the December
 2002 landslide (Tinti et al., 2006b).

The elicitation outcomes, described in Tadini et al. (submitted), provide the primary inputs for assigning probabilities to the
 105 simulations of our simulation database. For each target question, the ELICIPY tool generated a set of 10,000 samples
 representing the uncertainty distribution of the expert pool. This set was constructed through a two-step random sampling
 procedure, repeated 10,000 times: first, an expert was randomly selected with a probability equal to their performance-based
 weight; second, a single value was drawn from that expert's individual probability distribution. The resulting collection of
 10,000 samples thus constitutes a set of equiprobable realizations of the combined expert judgment.

Table 1 provides a statistical summary of these sample sets, reporting their 5th, 50th, and 95th percentiles for the key questions
 110 used in this study: the number of TLs in the next 50 years (TQ3), the percentage of those occurring within the SdF (TQ4), and
 the percentage of TLs across different landslide initial positions and volume ranges (TQ16-TQ35). While this table offers a
 concise summary, our methodology directly utilizes the entire collection of 10,000 samples for each question to generate the
 probabilistic maps and curves. This approach ensures that the full range of elicited uncertainty - and not just a summary based
 on three percentiles - is propagated into the final hazard assessment. Note that for TQ20-TQ35, the values in Table 1 and the
 115 corresponding samples represent conditional probabilities (see Fig. 8 in Tadini et al., submitted): the probabilities used for the
 maps described in the following sections are recalculated as absolute probabilities by considering TQ3, TQ4 and TQ16-TQ19
 (see Section 2.3.2).

120 **Table 1.** Percentile values for TQ3-4 and TQ16-35 for the CM scoring method for TLs in the next 50 years (from Tadini et
 al., submitted)

Question (unit)	5 th	50 th	95 th
TQ3: TLs at Stromboli (n°)	1	4	10
TQ4: TLs along the SdF (%)	66	82	96
TQ16: TLs along the SdF, initial position 700-300 m b.s.l.	2	12	37
TQ17: TLs along the SdF, initial position 300-0 m b.s.l.	4	28	58



TQ18: TLs along the SdF, initial position 0-300 m a.s.l.	5	21	52
TQ19: TLs along the SdF, initial position 300-700 m a.s.l.	7	31	62
TQ20: TLs along the SdF, initial position 700-300 m b.s.l., volume $1-5 \times 10^6 \text{ m}^3$ (%)	9	39	69
TQ21: TLs along the SdF, initial position 700-300 m b.s.l., volume $5-14 \times 10^6 \text{ m}^3$ (%)	6	26	57
TQ22: TLs along the SdF, initial position 700-300 m b.s.l., volume $14-30 \times 10^6 \text{ m}^3$ (%)	3	17	49
TQ23: TLs along the SdF, initial position 700-300 m b.s.l., volume $> 30 \times 10^6 \text{ m}^3$ (%)	0.3	9	37
TQ24: TLs along the SdF, initial position 300-0 m b.s.l., volume $1-5 \times 10^6 \text{ m}^3$ (%)	12	44	71
TQ25: TLs along the SdF, initial position 300-0 m b.s.l., volume $5-14 \times 10^6 \text{ m}^3$ (%)	6	25	71
TQ26: TLs along the SdF, initial position 300-0 m b.s.l., volume $14-30 \times 10^6 \text{ m}^3$ (%)	3	14	41
TQ27: TLs along the SdF, initial position 300-0 m b.s.l., volume $> 30 \times 10^6 \text{ m}^3$ (%)	0.3	9	39
TQ28: TLs along the SdF, initial position 0-300 m a.s.l., volume $1-5 \times 10^6 \text{ m}^3$ (%)	13	46	75
TQ29: TLs along the SdF, initial position 0-300 m a.s.l., volume $5-14 \times 10^6 \text{ m}^3$ (%)	6	23	53
TQ30: TLs along the SdF, initial position 0-300 m a.s.l., volume $14-30 \times 10^6 \text{ m}^3$ (%)	2	12	44
TQ31: TLs along the SdF, initial position 0-300 m a.s.l., volume $> 30 \times 10^6 \text{ m}^3$ (%)	0.1	8	39
TQ32: TLs along the SdF, initial position 300-700 m a.s.l., volume $1-5 \times 10^6 \text{ m}^3$ (%)	9	44	75
TQ33: TLs along the SdF, initial position 300-700 m a.s.l., volume $5-14 \times 10^6 \text{ m}^3$ (%)	6	24	58
TQ34: TLs along the SdF, initial position 300-700 m a.s.l., volume $14-30 \times 10^6 \text{ m}^3$ (%)	2	13	48
TQ35: TLs along the SdF, initial position 300-700 m a.s.l., volume $> 30 \times 10^6 \text{ m}^3$ (%)	0.1	7	42

2.2 Numerical simulations

To explore the epistemic uncertainties associated with tsunami modelling at Stromboli, this study relies on two distinct
 125 databases of numerical simulations, referred to as de' Michieli Vitturi et al. (2026a) and de' Michieli Vitturi et al. (2026b).
 These databases were designed to cover an identical matrix of landslide scenarios but were generated using different
 topobathymetric data and different landslide and tsunami numerical simulation model setups (code versions). All simulations
 were performed on a 21.9×23 km computational domain centred on Stromboli. The tsunamigenic source was modelled as the
 collapse of a granular mass placed on the existing topography. The geometry and position of the mass are defined by the
 130 horizontal coordinates of its barycentre (x_0 , y_0) and its length, width, and vertical thickness. These parameters collectively
 determine the landslide volume. In addition, the material's bulk density must be specified, typically as a water/material density
 contrast.

The simulations used in this paper represent a subset of those published in de' Michieli Vitturi et al. (2026a-b), and are done
 considering 11 initial barycentric positions along the Sciara del Fuoco centreline (P0-P10, see Fig. 1), two water/landslide
 135 density contrasts (0.5 and 0.6, corresponding respectively to material densities of 2000 and 1667 kg/m³) and 14 landslide



volumes (1, 1.5, 2, 3, 5, 8, 8.7, 11, 14, 17, 21, 25, 30 and $40 \times 10^6 \text{ m}^3$). Volumes 3, 5, 8.7, 14, 21 and $30 \times 10^6 \text{ m}^3$ are those already contained in Cerminara et al. (2024). For each database, we therefore considered a total of 308 simulations. The two simulation databases utilize different Digital Elevation Models (DEMs), representing one of the components of the epistemic uncertainty.

140 In de' Michieli Vitturi et al. (2026a) the topobathymetry is composed of:

- Topography obtained by elaborating the 3D point cloud acquired during an airborne LiDAR (Light Detection And Ranging) survey that was carried out in May 2012 (MASE, 2013). The data were acquired by using the Leica ADS80 sensor, which has instrumental vertical and horizontal accuracy of 0.10-0.20 and 0.25 m, respectively. The acquired point cloud had a mean point density of 8 pt/m^2 (Di Traglia et al., 2018).
- Bathymetry derived from the project Marine Geohazards along the Italian Coasts (MaGIC – Chiocci and Ridente, 2011). The MaGIC database consists of data with spatial resolution decreasing with depth, from 50 m to 100 and 200 m as the distance from the coast increases.

145

In de' Michieli Vitturi et al. (2026b), simulations use a more recent topobathymetry composed of:

- Topography obtained by elaborating 3D point cloud derived from a LiDAR (Light Detection And Ranging) survey conducted in 2023. The acquired data (Bisson et al., 2025) have a spatial resolution of 50 cm, an instrumental vertical accuracy of $< 5 \text{ cm}$, and a horizontal (planimetric) accuracy of $< 12 \text{ cm}$. The acquired point cloud had a mean point density with 4 to 6 pt/m^2 .
- Bathymetry from I.I.M.M. (Istituto Idrografico Marina Militare - Italian Navy Hydrographic Institute) with a resolution of 1 m from a depth of 3–4 m down to 60 m, and a resolution of 30 m from 60 m down to depths between 1000 and 1600 m.

150

155

The topographic and bathymetric data were then merged and resampled to 10 m, and a kriging interpolation was applied to fill the missing bathymetric portion between the shoreline and the beginning of the bathymetric data.

In general, a different spatial resolution of the DEM may result in a different inundation extent, with a loss of inundation detail but a larger inundation extent when using a lower resolution (e.g., Song and Goda, 2019). For our datasets, DEM resolution is not the only factor affecting the results. Indeed, although the DEMs of the two databases were both resampled to comparable grid resolutions (20 m and 10 m), an inspection of the original source data reveals substantial differences in the information content of the two topobathymetries. In particular, analysis of the 10 m versions highlights a clear contrast between the old and the new topobathymetry. For the bathymetric domain, the new version is characterized by a markedly higher native resolution and by more recent survey data, resulting in a significantly more detailed and accurate representation of the submarine morphology. This difference is already evident before any resampling procedure and directly affects the simulated tsunami wave propagation in the near-field marine environment. On land, the differences between the two datasets are of a different nature. The original data of both DEMs include the buildings, but the use of a 20 m resolution smooths them a lot. In addition, while the new topographic data are more recent, they are not filtered for vegetation. Therefore, trees (particularly tall vegetation) are retained in the DEM and appear as topographic obstacles with dimensions comparable to the tree canopy. This

160

165



170 feature represents a major difference in the source data used for the simulations. The older topography, in contrast, is effectively smoother, because of both the vegetation filtering and the lower resolution. This must therefore be considered when interpreting the effects of the adopted DEM on the simulated inundation patterns discussed in the following sections.

The simulations of both the databases were performed using Multilayer-HySEA, a non-hydrostatic multilayer model capable of simulating the coupling between granular landslide motion and water dynamics on GPU architectures. A detailed description of the model and its validation can be found in Macías et al. (2021a, b) and Esposti Ongaro et al. (2025). To reflect the evolution of modelling tools and to account for epistemic uncertainty related to the numerical solver, this study employs two distinct versions of the code, referred to here as the “2021 version” and the “2025 version”. The first one corresponds to the stable release available at the beginning of this study and used in previous hazard assessments at Stromboli (Esposti Ongaro et al., 2025), which represents a consolidated benchmark for simulating TLs in this volcanic setting.

180 The updated one introduces the following key improvements:

- **Improved Numerical Stability.** A new Riemann solver has been implemented. This enhancement stabilizes the numerical scheme, allowing for larger and more consistent time steps throughout the simulation and thus improving computational efficiency.
- **More Accurate Incompressibility.** The iterative solver enforcing the zero-divergence condition (i.e., fluid incompressibility) has been refined. It now employs a local convergence criterion, leading to a more robust and physically accurate solution, especially in complex flow conditions.
- **Layer-Independent Friction and Run-up.** A vertical linear viscosity model and a corrected formulation for the Manning friction have been introduced. Previously, friction was applied only to the bottom layer, making its total effect dependent on the number of layers used to discretize the water column. These new mechanisms ensure that the overall frictional dissipation and the resulting run-up behaviour are physically consistent and largely independent of the number of vertical layers chosen for the simulation.

The simulations contained in de’ Michieli Vitturi et al. (2026a), relying on the 20 m topobathymetry, were performed using the 2021 version of the numerical model, as done for the comprehensive analysis presented in Esposti Ongaro et al. (2025). The simulations presented in de’ Michieli Vitturi et al. (2026b) were carried out combining the updated 2025 version of the model with the more recent 10 m topobathymetry, leading to a database of scenarios based on improved numerical tools and higher-resolution data. In this work, we intentionally present and compare both datasets. The objective is not simply to supersede the previous results, but to highlight how model developments and new topographic data can influence hazard assessments. Moreover, as discussed in the final section, the newer dataset also presents some limitations (e.g. vegetation effects and partial resolution of urban features), and therefore cannot be considered consistently more accurate. Presenting both databases thus provides a more transparent view of the epistemic uncertainties associated with tsunami inundation modelling at Stromboli and frames the results within the context of evolving modelling capabilities. For the sake of brevity, and referring to their primary distinguishing feature, in the remainder of this paper we will refer to these two databases simply as the “Database A” (for de’ Michieli Vitturi et al., 2026a) and the “Database B” (for de’ Michieli Vitturi et al., 2026b).



2.3 Sensitivity analysis

205 To provide a first-order insight into the differences arising from the use of distinct Digital Elevation Models (DEMs) and numerical code versions, we performed a series of quantitative comparisons between pairs of simulations. These comparisons were designed to analyse separately the contributions of the topographic representation and of model developments, by varying one factor at a time. We focused on three key aspects of the inundation: the cell-by-cell water depth (in meters above ground), the overall inundated area, and the spatial agreement between the inundation patterns.

210 First, we conducted a direct, cell-by-cell comparison of the maximum water depth. The results are visualized through maps showing the absolute differences between two simulations, highlighting areas where one simulation predicts higher or lower water depths than the other. These maps are complemented by histograms that quantify the total area corresponding to specific intervals of water depth difference.

To quantify the spatial agreement between the inundated areas of two simulations (let's call them area A and area B), we employed the Jaccard index (J) and two complementary metrics, SIM_1 and SIM_2 .

215 The Jaccard index (Jaccard, 1901) measures the similarity between the two areas and is defined as the ratio of the intersection to the union:

$$J = \frac{|A \cap B|}{|A \cup B|}$$

220

A value of $J=1$ indicates perfect overlap, while $J=0$ means no overlap.

The SIM_1 and SIM_2 indexes quantify the portions of the total inundated area that are unique to each simulation, respectively:

$$SIM_1 = \frac{A \setminus B}{|A \cup B|}; SIM_2 = \frac{B \setminus A}{|A \cup B|}$$

225

For clarity, we use the subscript "TOT" when these indexes refer to the entire island of Stromboli and STV when they refer exclusively to the Stromboli village. For example, J_{STV} represents the Jaccard index for the village area.

2.3 Methodological framework for probabilistic hazard assessment

2.3.1 Hazard curves, maps, and profiles

230

The two main types of products are hazard curves (more commonly known in statistics as survival functions), which quantify the hazard at specific points, and hazard maps, which provide a spatial representation of the hazard across the entire domain. A hazard curve provides a more complete information at a specific location regarding the hazard model. A hazard map provides

an overview for a fixed level of the spatial variability and correlations which the hazard model features. Both maps and curves
235 have been produced considering a temporal framework of 50 years in the future, consistent with the outputs of the expert
elicitation (Tadini et al., submitted) and in line with similar studies of PTHA (e.g., Gibbons et al., 2020; Basili et al., 2021).
Hazard curves quantify, at a given location, the probability of exceeding different water depth thresholds, thus providing a
quantitative site-specific hazard assessment. For practical purposes, we present and discuss these curves only for a selection
of pre-defined points of interest.

240 The probabilistic inundation maps fall into two complementary categories:

- Probability of Exceedance Maps. For a given water depth threshold (e.g., 0.5 m), this product visualizes the
probability that the threshold will be exceeded at least once over the next 50 years. Because this probability is itself
uncertain due to epistemic uncertainties in source parameters (see Tadini et al., submitted), we do not produce a single
map but rather a distribution of possible outcomes. We present summary maps corresponding to different percentiles
245 (e.g., 5th, 50th, and 95th) of this probability distribution. Each pixel in a given percentile map thus represents that
specific level of confidence for the 50-year exceedance probability.
- Inundation Depth Maps for a Given Probability. Similarly, for a given 50-year probability of exceedance (e.g., 10%),
this product shows the corresponding inundation depth. This depth is also uncertain. Consequently, we present
percentile maps (5th, 50th, and 95th) that illustrate the range of possible inundation depths for that specific probability
250 level. Each pixel's value in these maps represents the water depth that has the specified probability of being equalled
or exceeded at least once over the next 50 years, at a given confidence level (percentile).

These two map types can be understood as different views of the underlying hazard curve computed for each pixel. A
probability exceedance map is equivalent to taking a vertical slice through the hazard curves at a fixed water depth and plotting
the corresponding probabilities. Conversely, an inundation depth map is equivalent to taking a horizontal slice at a fixed
255 probability and plotting the corresponding water depths.

The maps produced and shown in the following sections refer to specific water depth values, probabilities, and percentiles.
These values are as follows:

- water depth heights: 0.1, 0.2, 0.5 and 1 m. The use of water depth (or inundation/flow depth) to derive hazard maps
and curves has already been used in other tsunami hazard studies, for instance in Lorito et al. (2015) and Woessner
260 and Farahani (2020). In this latter study, water depth thresholds of 0.5, 1, 5 and 10 m are chosen based on engineering
considerations and fragility/vulnerability functions. For our Stromboli study case, we also used smaller thresholds
(0.1 and 0.2 m) to take into account the small scale of the investigated area. We also note that 0.5 m water depth is
potentially capable of dragging away adults (Kurusu et al., 2018);
- probabilities: 2% and 10%. These values have been used in other tsunami probabilistic hazard assessment studies
265 (e.g., Gibbons et al., 2020; Fukutani et al., 2021; Ramos et al., 2025);



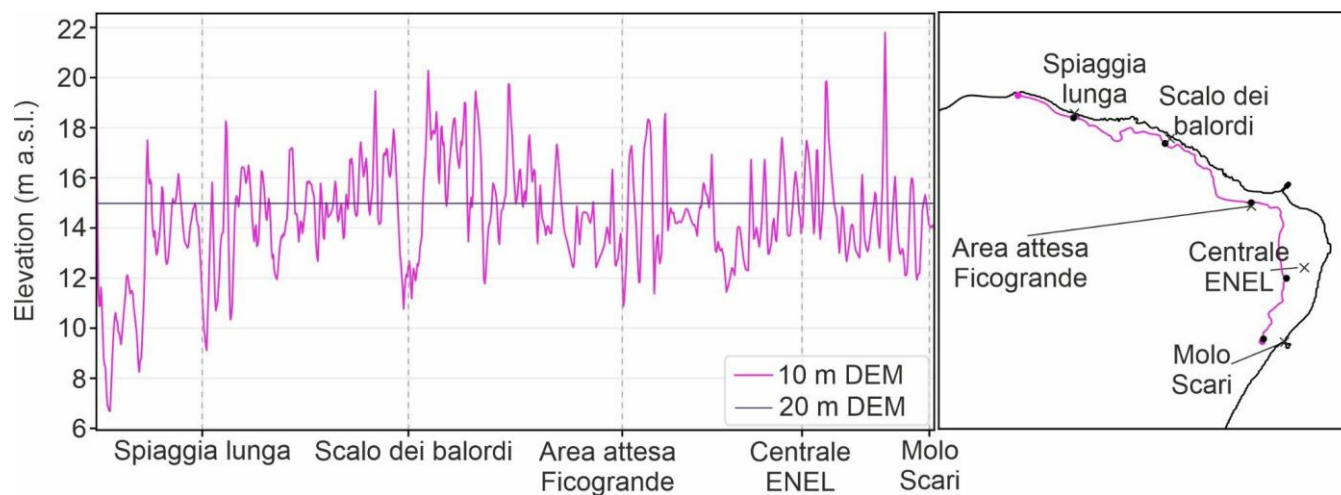
- percentiles: 5th/50th/95th. We chose these percentiles to be consistent with the outputs of the elicitation (Table 1 and Tadini et al., submitted), although in similar PTHA studies slightly different values are used (e.g., 2nd, 50th, 98th in Gibbons et al., 2020);
- 6 specific sites, chosen to be representative of the most critical points for infrastructures or from a touristic point of view (Figure 1). In particular, we have chosen the two main piers at the two villages of Ginostra and Stromboli (“Molo Ginostra” and “Molo Scari”, respectively), the main power plant of the island (“Centrale ENEL”), two touristic beaches (“Spiaggia Lunga” and “Scalo dei Balordi”) and a signal for waiting area positioned by Italian Civil protection in a safe area outside the inundation of the 2002 tsunami (“Area di attesa Ficogrande”; Bonilauri et al., 2021).

270

275

280

To generate the probabilistic maps for a fixed water depth threshold, those corresponding to a given exceedance probability and the hazard curves, we follow a procedure in line with standard PTHA methodologies (e.g., Grezio et al., 2017; Volpe et al., 2019; Selva et al., 2021). The full approach is described in Text S1 from Supporting Information. In addition to hazard curves and maps, we extracted hazard profiles from the probabilistic inundation maps to analyse in detail the hazard variability within Stromboli village. The profiles were sampled on the 20m DEM along the 15-m isohypse, which Bonilauri et al. (2021) proposed as a potential lower boundary of the tsunami safe zone. That contour was derived from the maximum runup of the 2002 tsunami (roughly along the 10-11 m isoline; Tinti et al., 2006a), with an added uncertainty margin of 5 m. To ensure a consistent comparison between model setups, the same contour line was used to extract hazard profiles from both the Database A and Database B results. Elevation differences between the two DEMs along this line are shown in Figure 2.



285

Figure 2. Left: Topographic profile extracted from the 10m DEM (purple line) along the 15 m isoline of the 20m DEM (blue line). Vertical dashed lines correspond to the closest point along the 15 m isoline (black dots in the map to the right) to 5 out of 6 sites where hazard curves have been developed (black crosses in the map to the right).



2.3.2 Integration with expert elicitation outcomes

290 The integration of elicited probabilities with the deterministic simulation database requires addressing two key methodological challenges:

1. Treatment of the unbounded volume interval, as the probability for landslides of class V4 (volumes $> 30 \times 10^6 \text{ m}^3$) does not have an upper limit.
2. Discretization of interval probabilities, as it is necessary to partition the probabilities of the position/volume intervals defined in the elicitation among the discrete scenarios that fall within or near each range in our simulation database.

295

Regarding point (1), we adopted two distinct approaches to address the unbounded nature of the highest volume class (V4, $> 30 \times 10^6 \text{ m}^3$), resulting in two separate sets of probabilistic maps and hazard curves:

- Approach A ($1-30 \times 10^6 \text{ m}^3$ volume range). This approach entirely excludes the V4 class from the analysis. The elicited probabilities for the three bounded volume ranges (1–5, 5–14, and $14-30 \times 10^6 \text{ m}^3$) were renormalized so that their sum equals 1. This method provides a probabilistic assessment conditional on the landslide volume in the range $1-30 \times 10^6 \text{ m}^3$.
- Approach B ($\geq 1 \text{ m}^3 \times 10^6 \text{ m}^3$ volume range). This approach includes the V4 class ($> 30 \times 10^6 \text{ m}^3$) by assigning its entire elicited probability to a single volume in this interval, which was chosen to be $40 \times 10^6 \text{ m}^3$. Although a simplification, this choice is consistent with both the power-law landslide scaling law described in Brunetti et al. (2009) and discussed for the Stromboli case in Tadini et al. (submitted), but also with the current modelling framework. Firstly, landslide volumes significantly larger than $40 \times 10^6 \text{ m}^3$, when initiated from higher elevations, would likely extend beyond the morphological boundaries of the Sciara del Fuoco, involving material that would not slide along its main path. Secondly, very large-volume failures might involve different triggering mechanisms, such as deep-seated rotational slides, which would require a different initial geometry (e.g., incised into the slope) rather than the 'on-top' placement used in our simulations.

300

305

310

Regarding point (2), we use the outputs of the CM method (see Section 2.1), that consist of a set of 10,000 probability values for each target question of Table 1. We also adopt a specific procedure to derive probabilities for each specific volume/position interval, which is extensively illustrated in Text S1 from Supporting Information. The core of this approach is to sample from each intervals a series of hypothetical scenarios (with a defined position/volume/density), and to map each of this scenario to the closet available simulation in the corresponding database subset (Figure 3 illustrate this mapping processes for the volume range $1-30 \times 10^6 \text{ m}^3$). The probability of each interval is then equally partitioned among the hypothetical scenarios that fall within each interval.

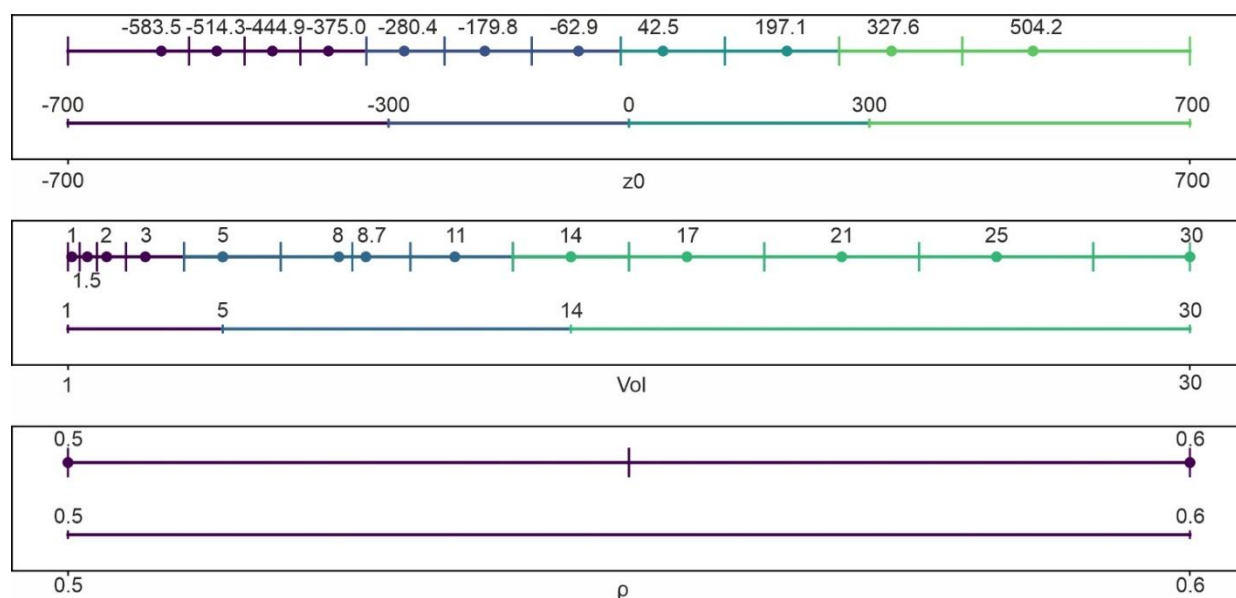
315

320

The final output of this procedure consists of two distinct sets of probability vectors, each containing 286 (volume range $1-30 \times 10^6 \text{ m}^3$) or 308 (volumes $\geq 1 \times 10^6 \text{ m}^3$) probability values.



325 The probabilities derived so far are conditional on the occurrence of a single tsunamigenic landslide within the SdF. To convert these into absolute probabilities over a 50-year time horizon, we account for the expected frequency of events by incorporating the 10,000 sampled values from elicitation questions TQ3 (number of events in 50 years, N_{50}) and TQ4 (percentage within the SdF, P_{SdF}). For each of the 10,000 sampling steps, we compute the expected number of events as $n = N_{50} \times P_{SdF}$ and then calculate the corresponding 50-year exceedance probability at every pixel. Because n is generally not an integer, we approximate its effect using the two nearest integers, N_{low} and N_{up} . The single-event conditional exceedance probability at each pixel is first used to compute the probabilities, as $[P(k) = 1 - (1 - p)^k]$, of at least one exceedance assuming N_{low} and N_{up} , respectively. The final 50-year exceedance probability is then obtained as a weighted average of these two values. Repeating 330 this procedure for all 10,000 realizations yields a distribution of 10,000 values for the 50-year exceedance probability at each pixel.



335 **Figure 3** Comparison between positions (z_0 – top panel), volumes (Vol – middle panel, $1-30 \times 10^6 \text{ m}^3$ range) and density contrast (ρ – bottom panel) for the simulations (upper straight line in each panel) and the ranges derived from the elicitation (lower straight line in each panel). For all upper straight lines, each simulated position/volume/density is marked by a circle, while the vertical lines indicate the segments (of the lower straight lines) associated with the corresponding circle (during the sampling of z_0 , Vol, and ρ).

340



3 Results

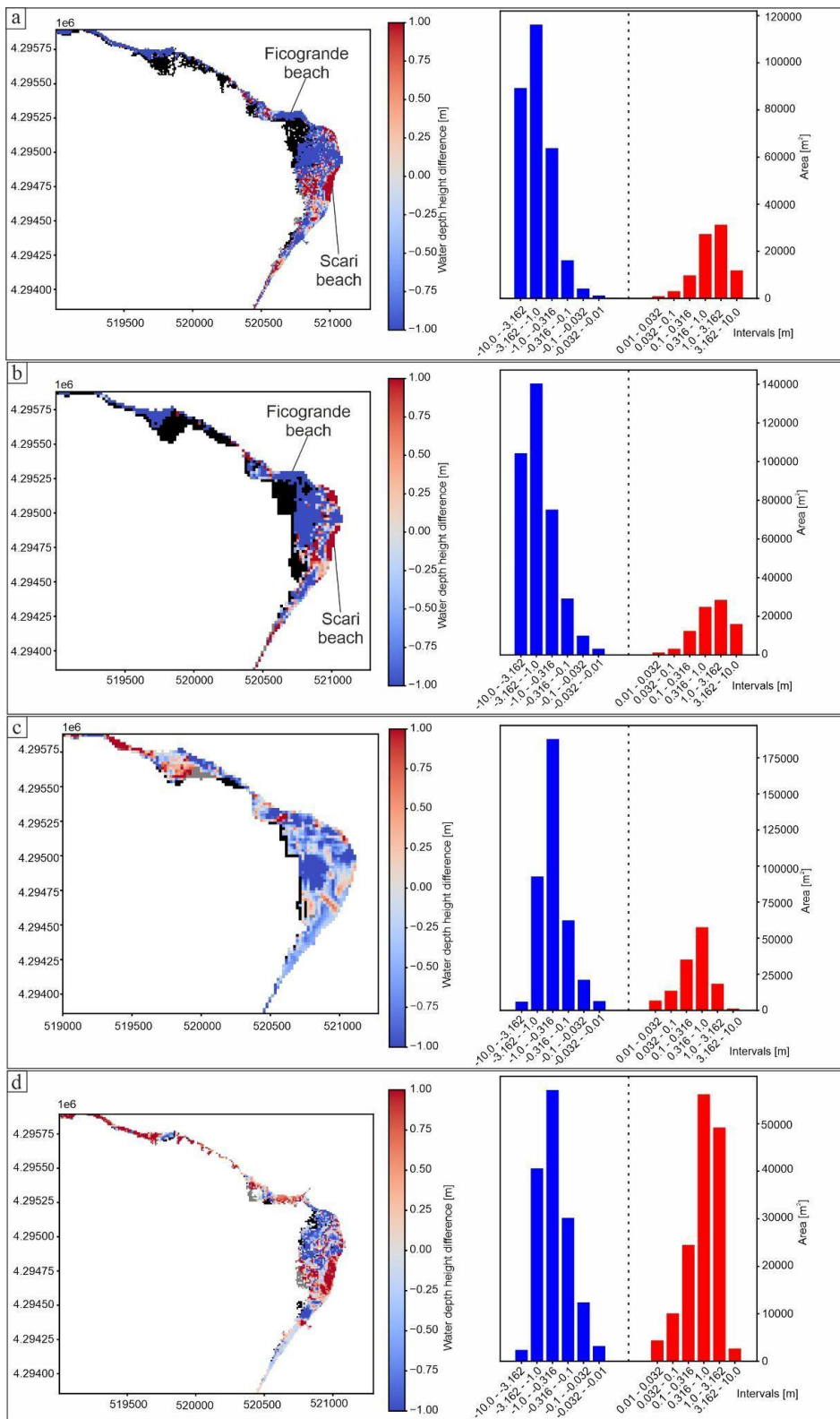
3.1 Sensitivity of inundation to different DEM resolutions and code versions

To assess the differences arising from the use of distinct Digital Elevation Models (DEMs) and numerical code versions separately, we performed few comparisons related to a single scenario, that is a large-volume landslide ($30 \times 10^6 \text{ m}^3$) with a density of 2000 kg/m^3 , originating from a high-elevation subaerial position (P0). This scenario was chosen as it produces one of the most significant inundations and is therefore well-suited to highlight the differences between the model setups. The analysis focuses on the inundation within the Stromboli village and combines qualitative observations of the maps (Figure 4) with quantitative assessments from Jaccard indexes (Table 2) and water depth difference histograms.

The main differences are observed when using the same version of the code (2021 version) and comparing the old and new DEMs, both at 10m (Fig. 4a) and at 20m (Fig. 4b) resolutions. The inundation map for these cases reveals a complex pattern of differences. Firstly, within the commonly inundated area, two fundamentally divergent behaviours are evident, represented by the intense red and blue colours. These indicate large zones where the water depth differs by several meters between the two simulations. The corresponding histogram confirms this divergence, showing a strongly bimodal distribution with peaks in the $[-3.16, -1.0] \text{ m}$ and $[1.0, 3.16] \text{ m}$ bins. In addition to these differences in water depth, a second critical feature is the presence of extensive black areas, which indicate that the OLD DEM produces a much larger inundation footprint, especially in the inland portions of the village. A major contribution to these differences comes from the changes in the coastline occurred in the time span between the two DEMs acquisition, which is particularly evident for the Ficogrande and Scari beaches. It is interesting to observe that, despite for both the locations a significant erosion occurred, for Ficogrande this results in a decrease in the maximum water depth (which also prevents the inundation of the area behind, shown in black in Figure 4a and 4b), while for Scari the erosion results in an increase in maximum water depth (red in Figure 4a and 4b). Differences in inundation for the Stromboli village are quantitatively confirmed by the Jaccard index ($J_{\text{STV}} = 0.645$ at 20m, 0.709 at 10m), which indicates poor spatial agreement, and by the fact that the area inundated exclusively by the OLD DEM amounts to either 27.0% (10m) or 34.3% (20m) of the total. Conversely, areas inundated only by the NEW DEM are negligible (1.2% at 20m and 2.1% at 10m).

In contrast, the impact of updating the numerical code from version 2021 to 2025 is more subtle, though still significant. On the same 20m DEM (Fig. 4c), the two code versions produce very similar inundation patterns, as confirmed by a high Jaccard index ($J_{\text{STV}} = 0.917$). The older 2021 version has a slightly larger footprint, inundating an exclusive area of just $31,451 \text{ m}^2$ (6.1%), which appears as thin black lines at the inundation margins. The water depth differences are also modest, with the histogram showing peaks for differences in the range of tens of centimetres.

However, the effect of the code update becomes much more pronounced on the 10m NEW DEM (Fig. 4d). While the difference in inundated area remains small (the 2021 version inundates an exclusive area of $16,225 \text{ m}^2$, or 5.5%), the impact on water depth is substantial. The histogram for this case has more pronounced peaks in the $[-3.16, -1.0] \text{ m}$ and the $[3.16, 1.0] \text{ m}$ bins.





375 **Figure 4** Comparison between simulations. a) $P0-30 \times 10^6 \text{ m}^3$, 10m NEW vs 10m OLD; b) $P0-30 \times 10^6 \text{ m}^3$, 20m NEW vs 20m
 OLD; c) $P0-30 \times 10^6 \text{ m}^3$, two versions of the code for 20m OLD DEM; d) $P0-30 \times 10^6 \text{ m}^3$, two versions of the code for 10m
 NEW DEM. For maps in left panels, grey pixels indicate areas where SIM_1 invades and SIM_2 does not invade, while black
 pixels indicate areas where SIM_2 invades while SIM_1 does not invade. In the right histograms, the vertical dashed line separates
 380 blue bins, where the water depth of SIM_1 is smaller than that of SIM_2 (i.e. negative difference), and red bins, where the water
 depth of SIM_1 is larger than that of SIM_2 (i.e. positive difference). Please note that the vertical scales for the histograms are
 different, while the horizontal bins are the same for all the plots.

Table 2 Jaccard indexes to compare different simulations for Stromboli Island (TOT) and Stromboli village (STV). In the first
 column, “OLD” refers to the DEM used in de’ Michieli Vitturi et al. (2026a) (both at its 20 m resolution and at 10 m resolution,
 385 obtained before the downsampling described in Section 2.2), while “NEW” refers to the DEM used in de’ Michieli Vitturi et
 al. (2026b) (both at its 10 m resolution and at 20 m resolution, obtained with a downsampling)

DEM	Code version	AREA AB Island/village	J _{TOT}	J _{STV}	SIM _{1,TOT}	SIM _{1,STV}	SIM _{2,TOT}	SIM _{2,STV}
Sim ₁ : 10 m (NEW) Sim ₂ : 10 m (OLD)	Sim ₁ : 2021 Sim ₂ : 2021	723,800 m ² / 379,400 m ²	0.740	0.709	0.036	0.021	0.224	0.270
Sim ₁ : 20 m (NEW) Sim ₂ : 20 m (OLD)	Sim ₁ : 2021 Sim ₂ : 2021	773,200 m ² / 457,600 m ²	0.663	0.645	0.057	0.012	0.280	0.343
Sim ₁ : 20m (OLD) Sim ₂ : 20m (OLD)	Sim ₁ : 2025 Sim ₂ : 2021	866,800 m ² / 515,600 m ²	0.909	0.917	0.020	0.022	0.071	0.061
Sim ₁ : 10m (NEW) Sim ₂ : 10m (NEW)	Sim ₁ : 2025 Sim ₂ : 2021	602,500 m ² / 295,000 m ²	0.906	0.888	0.043	0.057	0.051	0.055



3.2 Hazard maps, curves and profiles

390 3.2.1 Hazard maps with fixed water depth

Probabilistic maps for a fixed exceedance threshold of 0.5 m are presented in Figures 5 and 6. These two figures allow for a comparison of the combined effects of code version (2021 vs 2025), DEM resolution (20m vs 10m) and landslide volume range ($1-30 \times 10^6 \text{ m}^3$ vs $\geq 1 \times 10^6 \text{ m}^3$). With respect to the inundated areas, the effects of the different code versions are smaller than those resulting from the DEM resolution (see Section 2.2) and are not discussed here.

395 Despite the differences between these setups, all maps show a consistent overall hazard pattern. The area by far most exposed is the northeastern coast, where the main village of Stromboli is located. This is due to the combination of its exposure to tsunami energy diffracting from the Sciara del Fuoco (northwestern flank) and, crucially, its gentle coastal plain morphology, which allows for significant inland inundation. In contrast, other exposed coastlines like Ginostra (southwest) show a more limited hazard footprint due to their steeper topography. The hazard gradient is consistently sharp across the island; the
400 probability of inundation, represented by colours from yellow (high) to dark blue (low), decreases rapidly with increasing elevation away from the coast.

The comparison between the percentile maps within each row provides a powerful visualization of the uncertainty propagated from the expert elicitation. The 5th percentile map represents the lower uncertainty bound, while the Median map shows the central estimate. The 95th percentile map outlines a more severe, "1-in-20" case, meaning there is only a 5% chance that the hazard will be even greater. Although this represents a less probable outcome than the median, its likelihood is by no means
405 negligible, making it a useful reference for robust hazard assessment and risk mitigation planning. A critical result, common to all four setups, is that in the 95th percentile scenario, vast portions of the village's coastal area are coloured bright yellow. This indicates that, assuming such condition, these areas are almost certain to be inundated by at least 0.5 m of water over the next 50 years.

410 Beyond these general patterns, the figure allows for a detailed comparison of the impact of the different modelling choices. Regarding the effect of DEM resolution, as expected, these probabilistic results confirm the findings from the deterministic comparison shown in Figure 2. In both comparisons, the Database A (DEM resolution 20m, Fig. 5) produces a more extensive hazard footprint, with probabilities of inundation extending further inland compared to the Database B (DEM resolution 10m, Fig. 6). The 10m DEM, by resolving small-scale natural obstacles, confines the hazard more closely to the coastline, offering
415 a more accurate, albeit less conservative, depiction of the inundation extent.

Similarly, the effect of including larger volume landslides is evaluated by comparing Figure 5a-b and Figure 6a-b. In both cases, incorporating the $40 \times 10^6 \text{ m}^3$ scenarios (Figs. 5b and 6b) increases the overall hazard.

In summary, the most conservative hazard assessment, in terms of spatial extent and probability values, is provided by the setup in the Database A, $\geq 1 \times 10^6 \text{ m}^3$ range (Fig. 5b), while the least conservative is that of Database B, $1-30 \times 10^6 \text{ m}^3$ range
420 (Fig. 6a). Presenting this matrix of results is therefore essential for transparently communicating not only the tsunami hazard but also the significant uncertainty associated with key modelling choices.

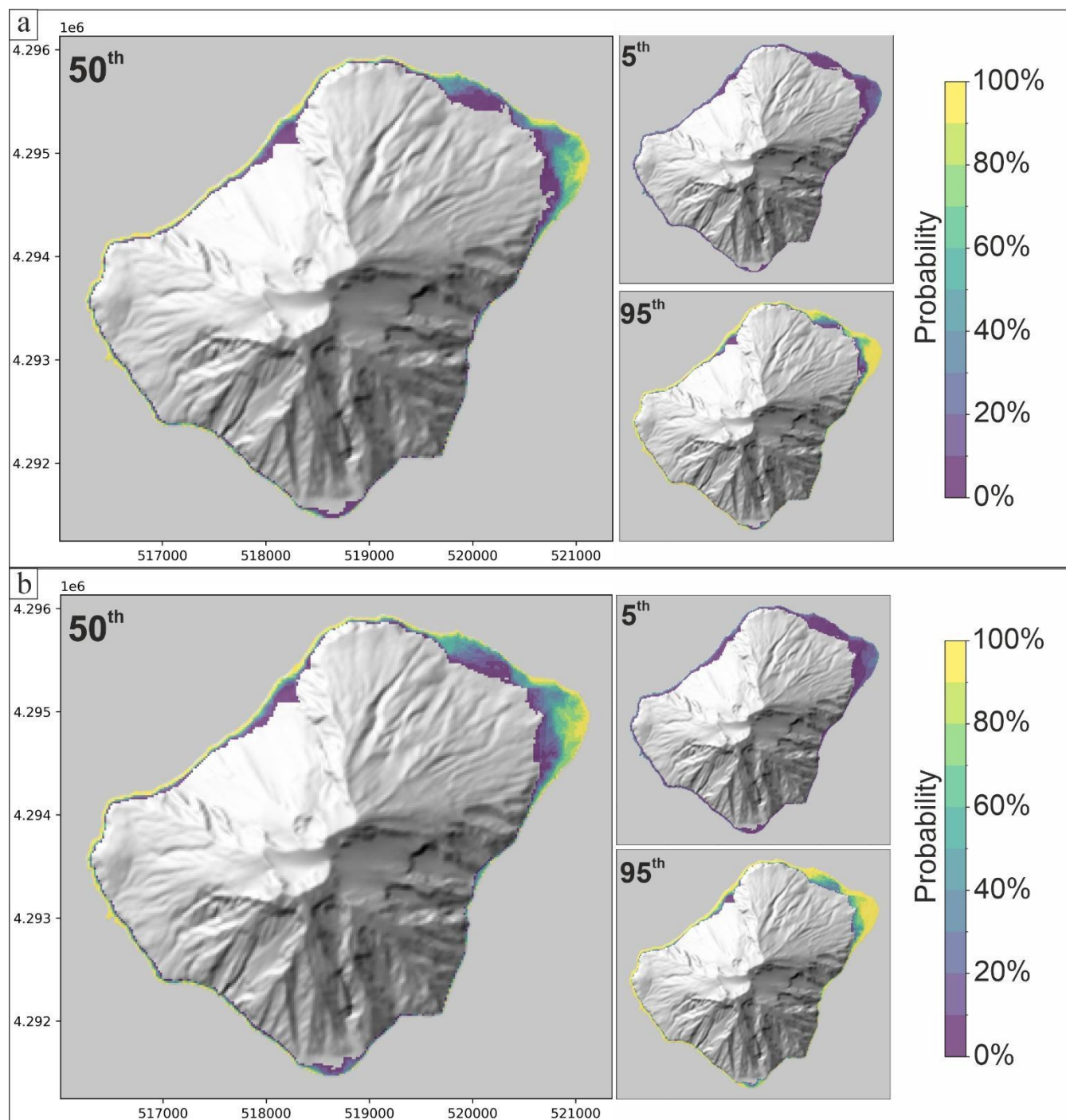


Figure 5. Probabilistic maps for exceeding a water depth of 0.5 m over a 50-year horizon for the Database A. (a) Volume range $1-30 \times 10^6 \text{ m}^3$; (b) volume range $\geq 1 \times 10^6 \text{ m}^3$.

425

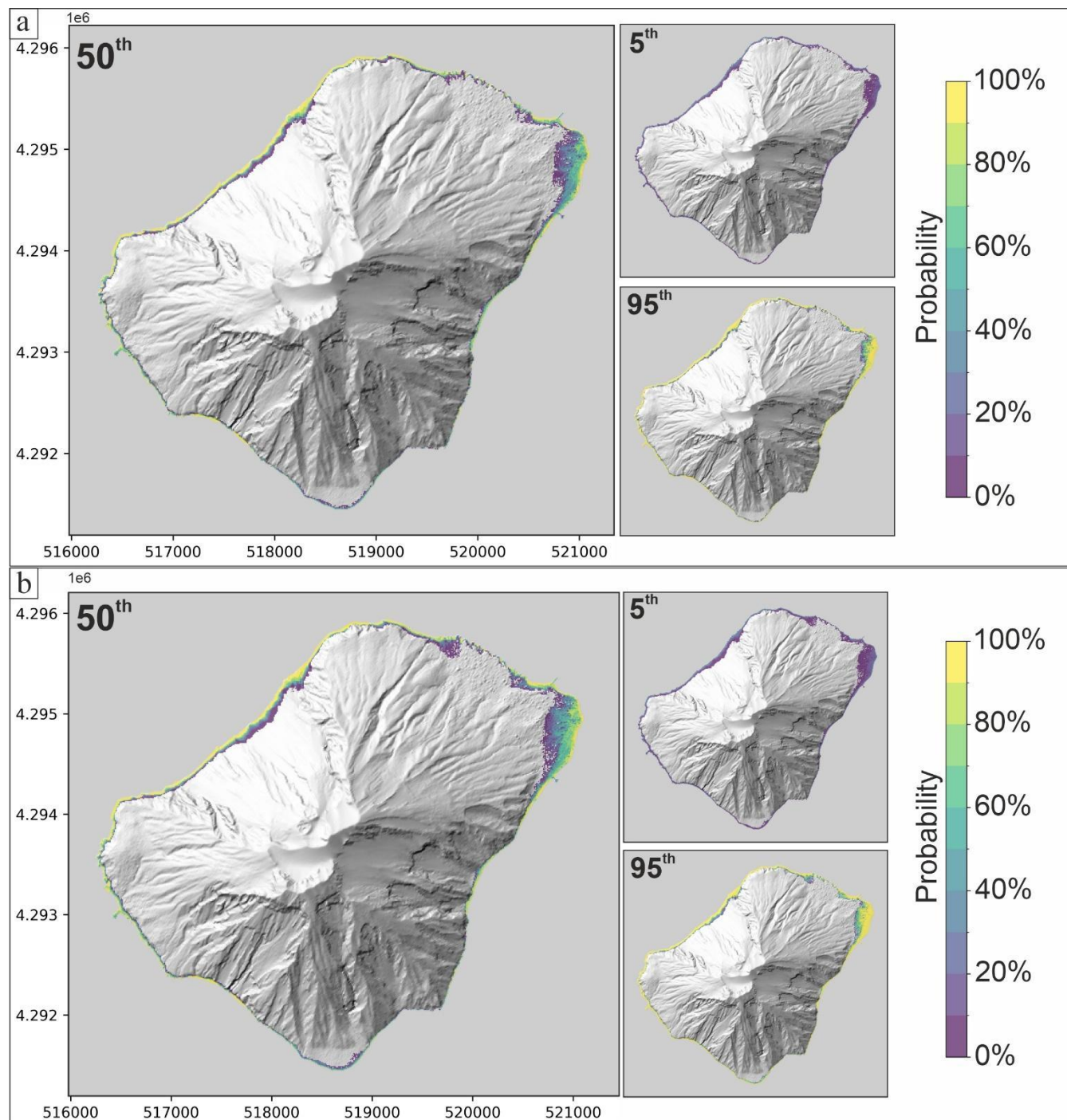


Figure 6. Probabilistic maps for exceeding a water depth of 0.5 m over a 50-year horizon for the Database B. (a) Volume range $1-30 \times 10^6 \text{ m}^3$; (b) volume range $\geq 1 \times 10^6 \text{ m}^3$.

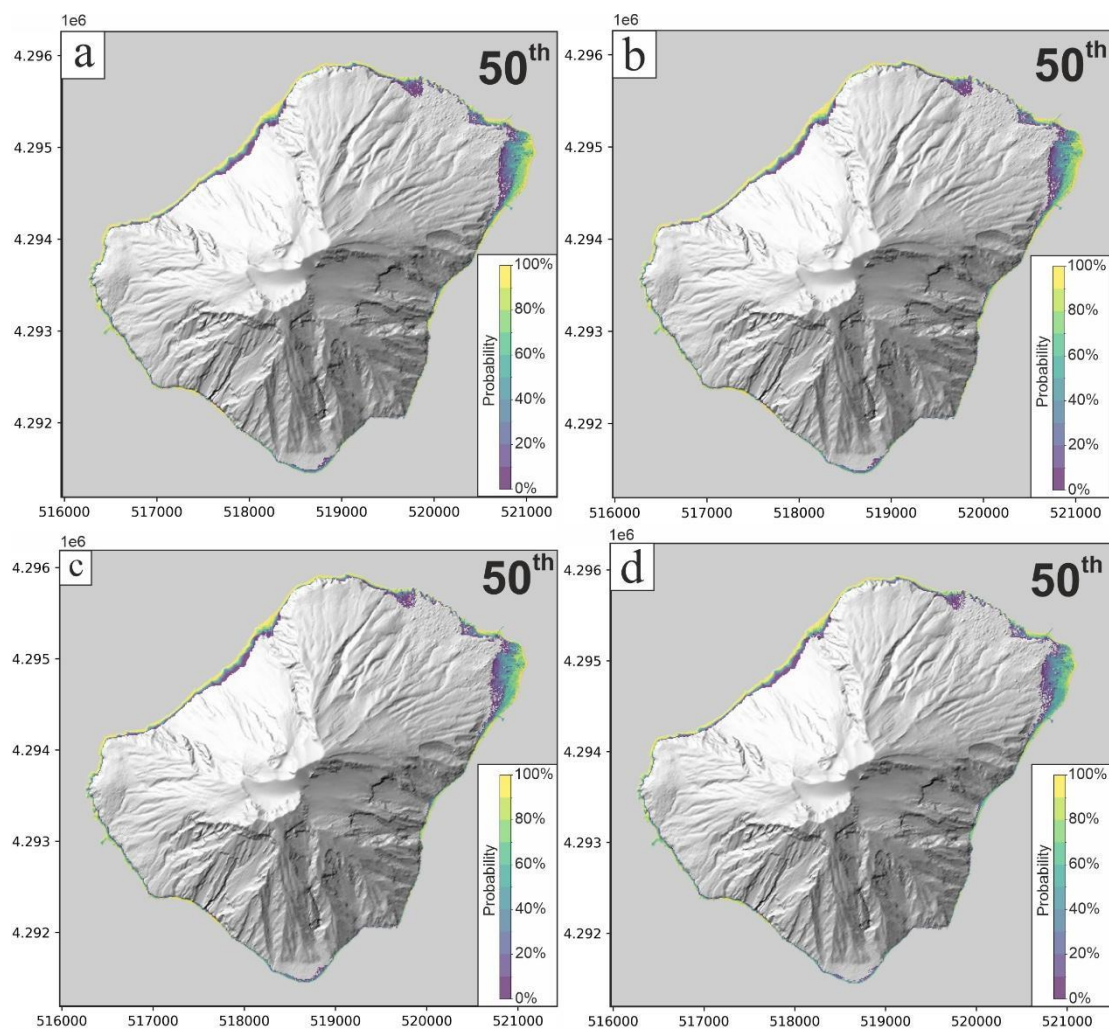


430

To further investigate the hazard, we analysed the sensitivity of the probabilistic maps to the chosen water depth threshold. Figure 7 illustrates this by comparing the 50th percentile probability map of the 0.5 m (Fig. 7c, same as Fig. 6b) for three different exceedance thresholds (Fig. 7a, b, d): 0.1 m, 0.2 m, and 1.0 m. These maps were all generated using a setup combining the Database B with the $\geq 1 \times 10^6 \text{ m}^3$ volume range. The full maps for these thresholds are displayed in Figs. S1-S6.

435

The comparison reveals a striking result: the overall footprint of the area with significant hazard probability remains remarkably stable, showing only minor contractions as the water depth threshold increases from 0.1 m to 1.0 m. Although subtle differences exist, with a slightly larger and more uniform hazard area for the 0.1 m threshold as expected, the primary boundaries of the inundated zone do not change substantially.





440 **Figure 7.** Sensitivity of the 50th percentile probabilistic inundation map to the water depth threshold. The maps show the 50-year probability of exceeding (a) 0.1 m, (b) 0.2 m, (c) 0.5 m, and d) 1.0 m, all for the Database B and $\geq 1 \times 10^6 \text{ m}^3$ volume range setup.

3.2.2 Hazard maps with fixed probability

The probabilistic inundation maps corresponding to a 10% exceedance probability in 50 years are shown in Figures 8 and 9.

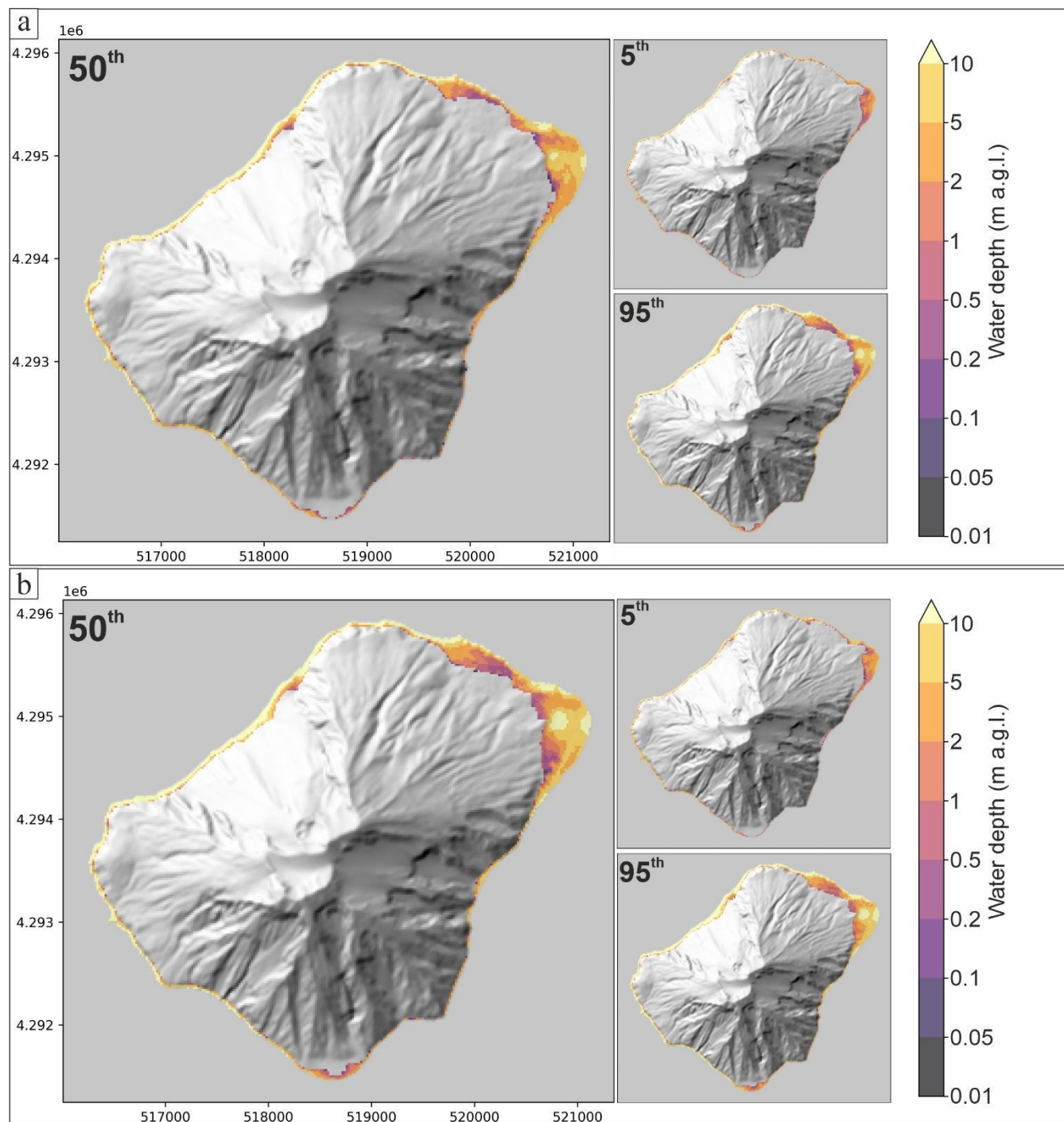
445 Those corresponding to the 2% exceedance probability are displayed in Figs. S7-S8 from the Supporting Information. This type of map is particularly useful for planning purposes as it visualizes the expected inundation intensity for a given likelihood level.

The three columns within each row effectively visualize the uncertainty associated with the water depth for this 10% probability level. The 5th percentile map represents a more moderate inundation scenario, with water depths generally below 1-2 meters even in the most exposed areas. The Median map shows a more significant inundation, with depths commonly exceeding 2 meters along the coast. The 95th percentile map depicts a far more severe scenario; for the same 10% probability, the expected water depths are higher, with water depth > 5 meters along the entire waterfront. This highlights the substantial uncertainty in the potential intensity of a "10% probability" event.

450 The most significant factor influencing the results is the DEM resolution, which primarily controls the spatial extent of the hazard. Comparing the maps generated with the Database A (20m DEM resolution, Fig. 8) to those with the Database B (10m DEM resolution, Fig. 9), it is evident that the former consistently produce a much larger inundation area for the same percentile and volume range. This effect is particularly pronounced in the 95th percentile maps, where the inundation from the Database A extends significantly further inland across the coastal plain. While the Database B provides a more heterogeneous and detailed inundation pattern, with corridors of deeper flow and shadow zones, its overall footprint is more constrained.

460 The inclusion of larger landslide volumes ($> 30 \times 10^6 \text{ m}^3$) also has a clear and significant impact, primarily on the intensity of the inundation. Comparing the results for the $1-30 \times 10^6 \text{ m}^3$ range (Figs. 8a and 9a) with those including the $40 \times 10^6 \text{ m}^3$ scenarios (Figs. 8b and 9b) reveals a striking increase in inundation severity. For the same 10% exceedance probability, the water depths in the lower two rows are significantly higher across all percentiles. The Median and 95th percentile maps, in particular, shift from showing predominantly 1-2 meters of water depth to > 5 meters of water depth. This demonstrates that including high-consequence events in the analysis drastically elevates the expected water depth for any given probability level.

465



470 **Figure 8.** Probabilistic maps showing the inundation water depth corresponding to a 10% exceedance probability over a 50-year horizon for the Database A. (a) Volume range $1-30 \times 10^6 \text{ m}^3$; (b) volume range $\geq 1 \times 10^6 \text{ m}^3$.

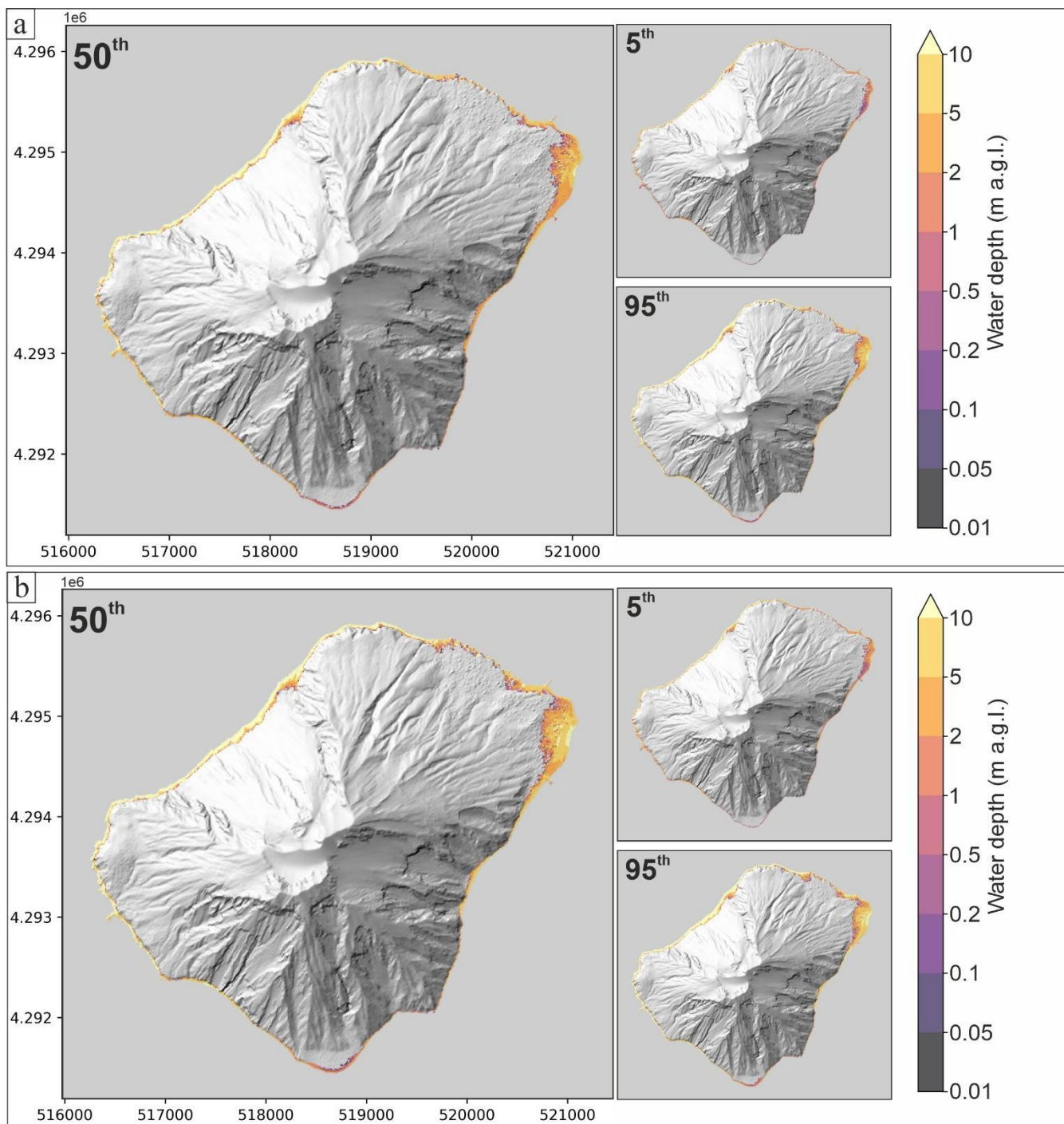


Figure 9. Probabilistic maps showing the inundation water depth corresponding to a 10% exceedance probability over a 50-year horizon for the Database B. (a) Volume range $1-30 \times 10^6 \text{ m}^3$; (b) volume range $\geq 1 \times 10^6 \text{ m}^3$.



480 To complete the analysis, we investigated how the expected inundation intensity changes for different levels of exceedance probability. Figure 10 compares the water depth maps for two different 50-year exceedance probabilities, 2% (Fig. 10a) and 10% (Fig. 10b), across all three statistical estimators: the 5th, 50th, and 95th percentiles (left, central, and right columns, respectively). All maps were generated using the most detailed setup (10m DEM with the $\geq 1 \times 10^6$ m³ volume range).

485 The results reveal a complex, non-uniform sensitivity that depends on the percentile considered. For the 50th percentile and 95th percentile maps (central and right columns in Fig. 10), a striking saturation effect is observed. The inundation intensity is remarkably insensitive to the chosen probability level, with the maps for 2% and 10% probability being nearly identical. This suggests that for the median and reasonably pessimistic scenarios, the upper tail of the hazard curve is very steep. Once the analysis includes high-consequence events, a significant decrease in probability (from 10% to 2%) does not correspond to a significant increase in the predicted water depth.

490 This dual behaviour has profound implications for hazard assessment. For the 50th and 95th percentile maps, the hazard appears to reach a plateau, meaning that planning for a 10% probability event may already provide robust protection against much rarer tsunamis, or the other way around, that is planning for a better protection may be worthwhile as it adds a limited marginal cost. For the 5th percentile maps, however, the severity continues to scale with the rarity of the event. This highlights the complex nature of the hazard distribution, where the uncertainty tails behave differently from the central tendency.

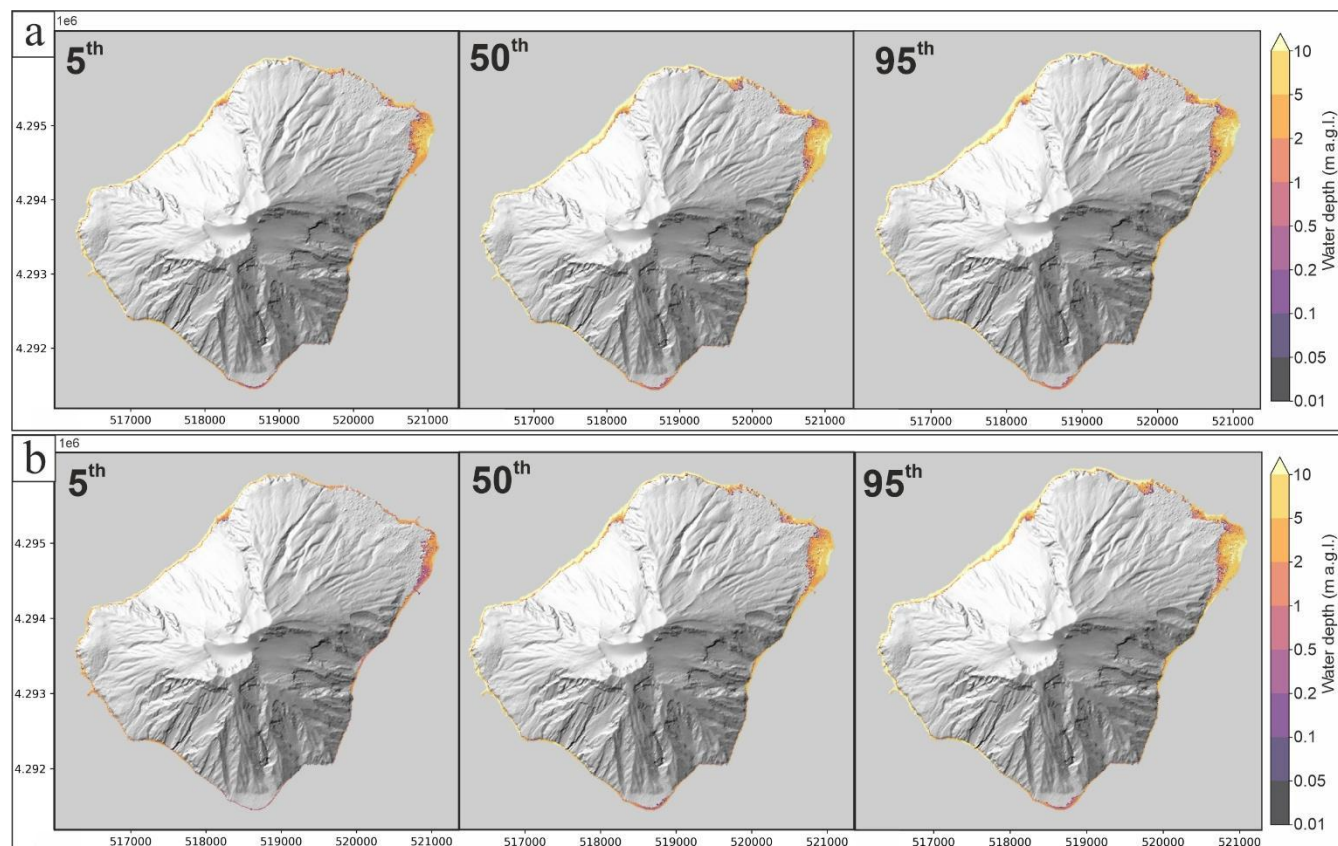


Figure 10. Effect of the exceedance probability level on the percentile inundation depth maps. All maps were generated using the 10m DEM with the $\geq 1 \times 10^6$ m³ landslide volume range. a) water depth for a 2% probability in 50 years; b) water depth for a 10% probability in 50 years.

3.2.3 Hazard Curves

A detailed, quantitative assessment of the tsunami hazard at specific locations is provided by hazard curves, which were generated for 6 points of interest around the island (see Fig. 1). In this section, we present and discuss the results for two representative sites within the Stromboli village: "Centrale ENEL", located directly on the waterfront and highly exposed, and "Area di attesa Ficogrande," situated further inland at a slightly higher elevation. In addition to their locations with respect to the coastline, they are interesting as they are the island power plant, and one of the assembly points to be used after evacuation, respectively. The hazard curves for these sites (Figures 11 and 12) plot the 50-year probability of exceeding a range of water depths and are presented for all four set of maps (Databases A and B and $1-30 \times 10^6$ m³ $\geq 1 \times 10^6$ m³ volume ranges), showing the 5th, Median, and 95th percentile results. The hazard curves for the additional sites shown in Figure 1 are provided in Figs. S9-S12 from the Supporting Information.



510 These curves provide a synthesis of the hazard and its associated uncertainty. The vertical distance between the 5th percentile (blue line) and the 95th percentile (green line) illustrates the wide range of uncertainty in the exceedance probability for a given water depth, which often spans more than an order of magnitude. Similarly, the horizontal distance between these curves quantifies the uncertainty in the inundation water depth for a given probability level. For example, at the Centrale ENEL site for a 10% exceedance probability, the expected water depth could range from approximately 2 meters (5th percentile) to over 6 meters (95th percentile), highlighting the vast range of plausible outcomes.

515 The shape of the curves, particularly the steepness of their "roll-off" at higher water depths, is fundamental to understanding the nature of the hazard. For the Centrale ENEL site (Figure 11), the Median and 95th percentile curves (orange and green lines) exhibit an extremely steep decay for low probabilities (<10%). This explains the "saturation effect" observed in the corresponding maps: in this steep portion of the curve, a large decrease in probability (e.g., from 10% to 2%) translates into only a minor increase in the associated water depth. Conversely, the 5th percentile curve (blue line) has a much gentler slope, explaining why for this percentile, a similar decrease in probability corresponds to a much more significant increase in expected water depth.

520 The effect of the DEM is particularly evident at the "Area di attesa Ficogrande" site (Figure 12). While the Database A (20m DEM) predicts a non-negligible hazard, the curves generated with the Database B (10m DEM - bottom panels) drop to near-zero probability for any significant water depth.

525 The effect of including larger landslide volumes is also clear and systematic. In all panels of both figures, the curves for the $\geq 1 \times 10^6$ m³ range (right columns) are consistently shifted to the right compared to those for the $1-30 \times 10^6$ m³ range (left columns). This indicates, as expected, a higher hazard level, where any given exceedance probability corresponds to a greater water depth when high-consequence events are included in the analysis. It is important to note that since the x-axis is on a logarithmic scale, even a visually moderate shift in the right-hand part of the graph corresponds to a significant increase in the absolute water depth, often on the order of several meters. This shift is pronounced across all percentiles, underscoring the substantial contribution of larger, rarer events to the overall hazard assessment.

530

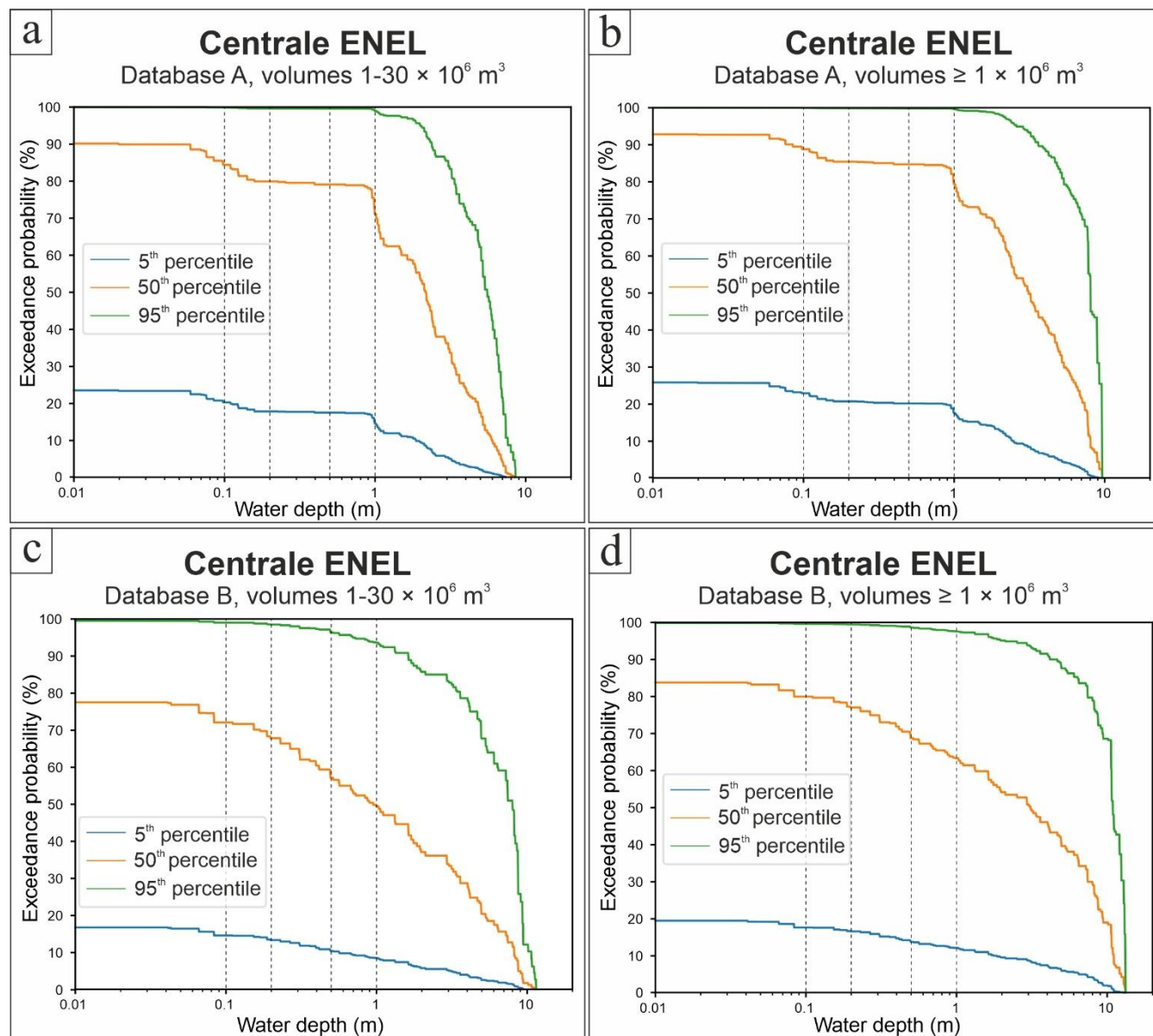


Figure 11. Probabilistic hazard curves for the "Centrale ENEL" site. The panels compare the results for the four different model setups: Database A (a-b), Database B (c-d), $1-30 \times 10^6 \text{ m}^3$ volume range (a-c), and $\geq 1 \times 10^6 \text{ m}^3$ volume range (b-d). Each panel shows the 50-year exceedance probability as a function of water depth for the 5th, 50th, and 95th percentiles of the hazard distribution. Vertical grey dashed lines correspond to the water depth thresholds used for map production (0.1, 0.2, 0.5 and 1 m).

535

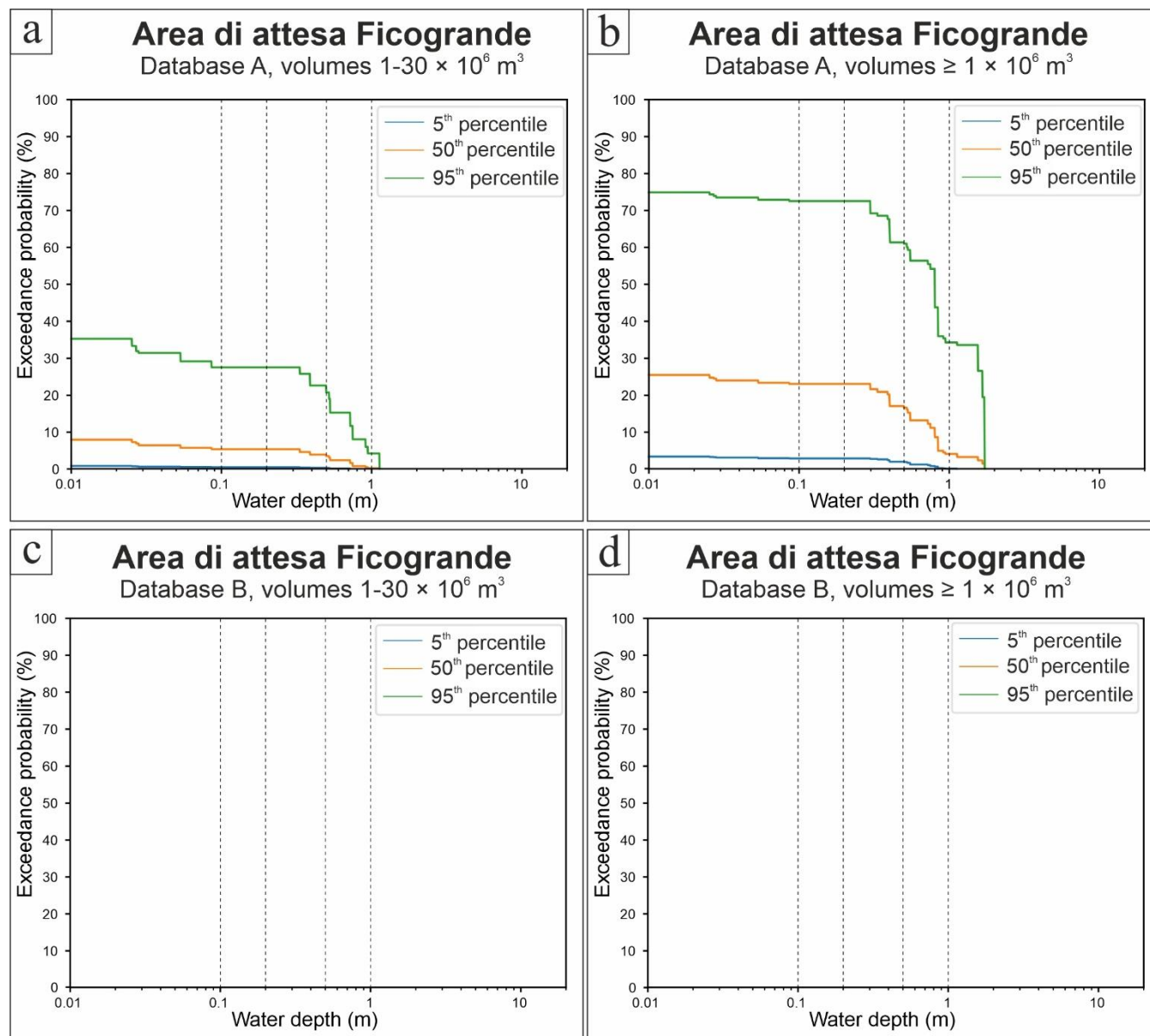


Figure 12. Probabilistic hazard curves for the "Area di attesa Ficogrando" site. The panels compare the results for the four different model setups: Database A (a-b), Database B (c-d), $1-30 \times 10^6 \text{ m}^3$ volume range (a-c), and $\geq 1 \times 10^6 \text{ m}^3$ volume range (b-d). Each panel shows the 50-year exceedance probability as a function of water depth for the 5th, 50th, and 95th percentiles of the hazard distribution. Note the drastic reduction in hazard for this inland site when using the Database B (c-d). Vertical grey dashed lines correspond to the water depth thresholds used for map production (0.1, 0.2, 0.5 and 1 m).

540



545 3.2.4 Hazard profiles

Regarding the hazard profiles (Figures 13-14), the values from the 2D probabilistic maps (5th, Median, and 95th percentiles) were interpolated at a high number of points along this contour to generate a continuous 1D representation of the hazard. In each panel of the resulting figures, the thin, oscillating line represents the direct result of the interpolation, while the thicker dashed line shows a smoothed version of the same profile, which helps to visualize the underlying trend by filtering out high-frequency noise. We stress that the sites corresponding to the hazard curves of Figs. 13-14 are not located along the 15 m isoline: rather, they are included just to provide an indication of the point along the isoline which is closest to the site of the hazard curve.

550 Figure 13 shows the resulting profiles for the probability of exceeding 0.5 m of water depth, comparing the Database A (Fig. 13a) with the Database B (Fig. 13b) both for the $\geq 1 \times 10^6 \text{ m}^3$ volume interval. These profiles reveal that the probability of significant inundation is consistently high within the village, though with some localized variations. A dip is observed along the segment between "Scalo dei Balordi" and "Area di attesa Ficogrande". A more subtle decrease is visible east of "Area di attesa Ficogrande" while a more significant and progressive drop in probability occurs in the easternmost section, from "Centrale ENEL" to "Molo Scari".

560 In contrast, the profiles showing the water depth for a fixed 10% exceedance probability (Figure 14) exhibit a greater variability. Here, a clear decreasing trend in water depth is visible moving from west to east, away from the area of direct impact of the waves generated at the Sciara del Fuoco. This trend is smoother and more evident in the profiles from the Database A (Fig. 14a), while it is superimposed with high-frequency oscillations in the profiles from the Database B (Fig. 14b).

565 A key difference between the two sets of profiles is the frequency of the oscillations, which directly highlights the impact of the DEM resolution. The profiles derived from the Database B (panel b in both figures) consistently exhibit high-frequency oscillations that are much more pronounced than in the profiles from the Database A (panel a). This is a numerical artifact originating from the interpolation procedure. As the profile is traced along the 15 m isobath, the bilinear interpolation samples values from the underlying discrete grid of the probabilistic map. Each oscillation corresponds to the path crossing from one set of four grid cells to the next. Since the 10m DEM has a finer grid, these crossings occur more frequently, resulting in the observed high-frequency noise. The 20m DEM, being coarser, produces a smoother profile with lower-frequency oscillations, as the path remains within the same set of interpolating cells for a longer distance.

570 Finally, the profiles provide a quantitative measure of the uncertainty along the selected isoline. The vertical distance between the 5th and 95th percentile curves is substantial in all cases, reinforcing the wide range of plausible outcomes derived from the expert elicitation. This is particularly evident in Figure 14, where the 95th percentile water depth is often several times greater than the 5th percentile value for the same 10% probability, underscoring the large uncertainty in the potential intensity of the inundation. It should be noted that, for the profiles obtained for a fixed probability (Figure 14), despite the resolution-induced differences in signal smoothness, the spatial position of the relative peaks (local maxima) along the 15 m isohypse remains



consistent between the two databases. This consistency indicates that the identification of the most exposed segments of the coast is robust and not heavily dependent on the specific model setup.

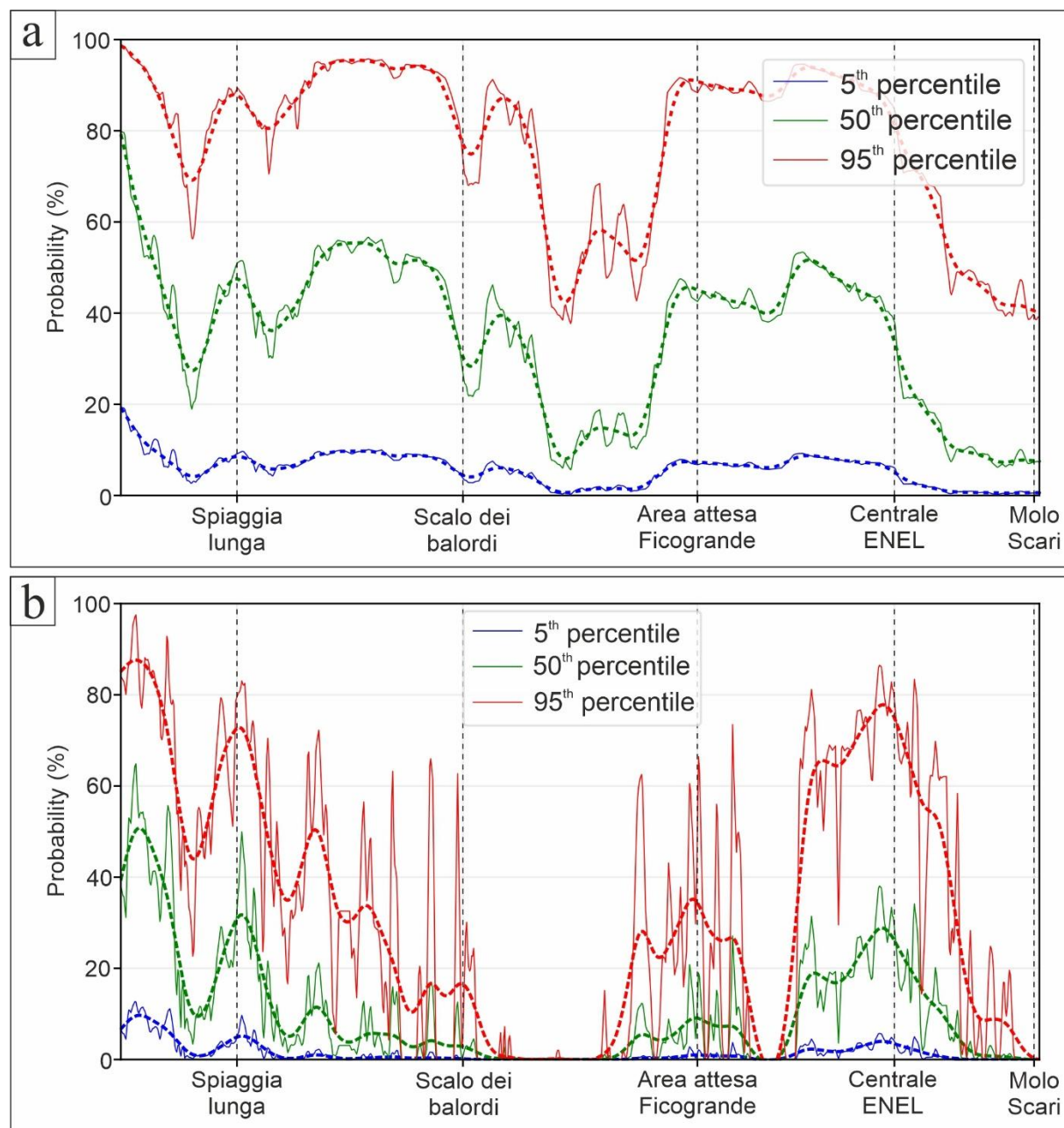
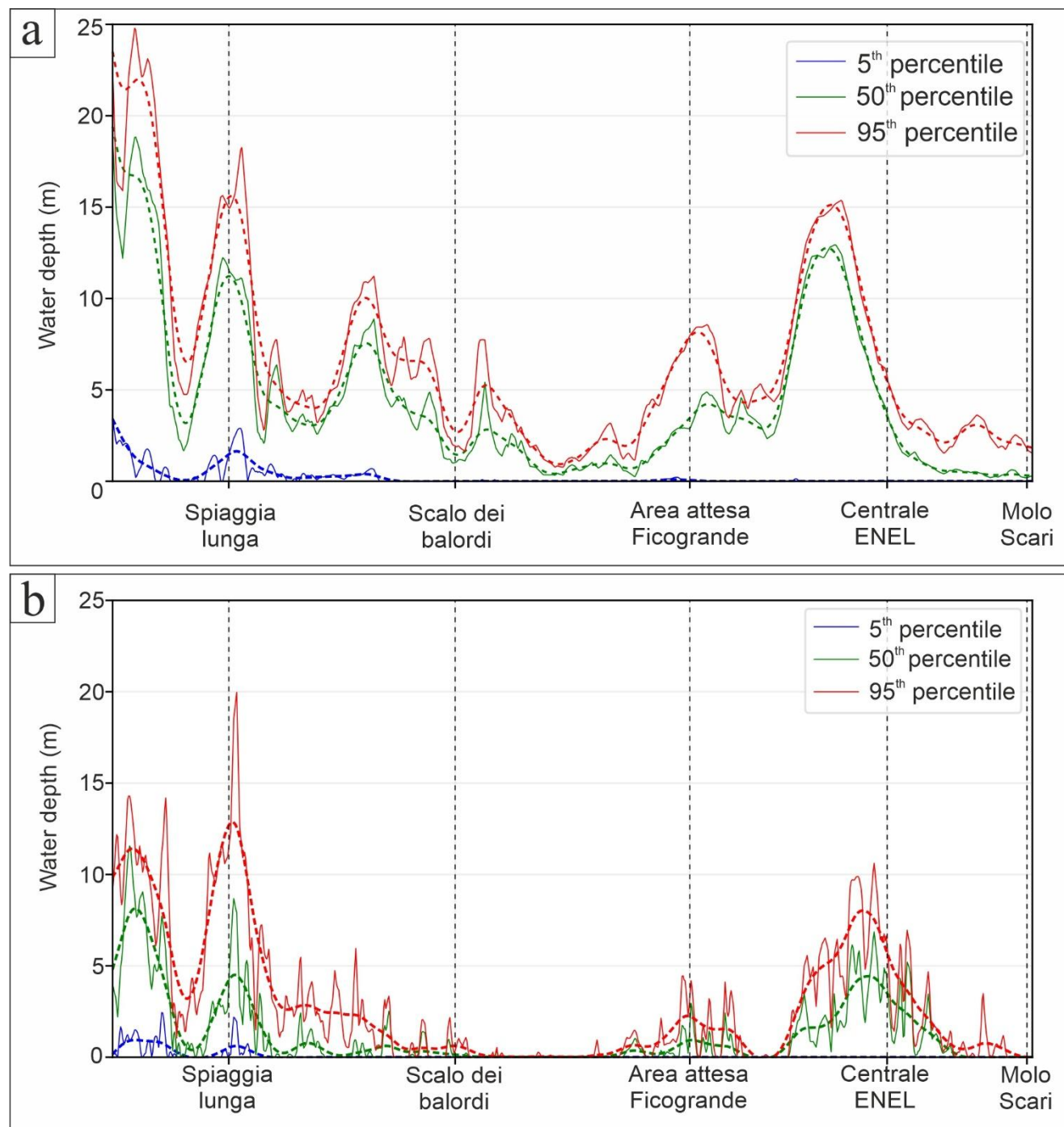


Figure 13. Profiles along the 15 m isoline of the 20m DEM (5th-50th-95th) for maps with water depth 0.5 m for a) Database A and b) Database B. Vertical dashed lines correspond to the closest point along the 15 m isoline (black dots in the map to the right) to 5 out of 6 sites where hazard curves have been developed (black crosses in the map to the right; see Section 3.4).

580



585

Figure 14 Profiles along the 15 m isoline of the 20m DEM (5th-50th-95th) for maps with probability 10% for a) Database A and b) Database B. Vertical dashed lines correspond to the closest point along the 15 m isoline to 5 out of 6 sites where hazard curves have been developed (see Section 3.4).



4 Discussion

590 This study presents a first PTHA for Stromboli Island, stemming from potential landslides on the Sciara del Fuoco. As indicated in the companion paper of Tadini et al. (submitted), the importance of this study lies in the current incompleteness of a full PTHA for Stromboli Island. While in fact a PTHA from seismic sources is available for the Mediterranean Sea (Basili et al., 2018; 2021), it is currently missing from local sources such as landslides induced by volcanic activity. This work therefore represents a first step toward a more comprehensive PTHA for Stromboli Island.

595 In this study, by integrating two large databases of numerical tsunami simulations with a structured expert elicitation, we have produced a suite of probabilistic inundation maps and hazard curves that quantify not only the expected hazard but also its associated uncertainty. The simulation databases were developed using high-resolution 20m and 10m topobathymetries and two versions of an advanced non-hydrostatic numerical model. The uncertainty in landslide source parameters—such as volume, initial position, and frequency of occurrence—was quantified through an expert elicitation and propagated through the entire hazard assessment workflow. This latter produced a series of probabilistic hazard maps presented as a set of three maps that help in quickly visualising the uncertainty. The incorporation of uncertainty in maps and curves is already established when dealing both with volcanic (see e.g. Neri et al., 2015; Constantinescu et al., 2022; Tadini et al., 2025) and tsunami hazard (see e.g., Glimsdal et al., 2019; Løvholt et al., 2020; Tonini et al., 2021). Following these approaches of quantitative hazard assessment, our approach includes:

- 605
- a quantification of both epistemic and aleatoric uncertainty through a formalized expert elicitation (considering the Cooke's Classical Model);
 - a modelling approach where a substantial set of simulations are developed in different databases (for sensitivity test with respect to DEM resolution and code version) and combined with the probabilities obtained from expert elicitation;
 - 610 ● a representation of uncertainty through different products (hazard maps, hazard curves and hazard profiles) that allow to carefully evaluate the hazard with respect to different locations.

4.1 Sensitivity of the results to the use of a different model version, DEM and landslide volume range

The combined use of the new, high-resolution 10 m DEM and the updated '2025 version' of the code (Database B) results in a systematically lower hazard estimate compared to the 20 m DEM and the '2021 code version' (Database A).

615 Regarding the use of different code versions, we can see a systematic effect: the new 2025 code version leads to a significant reduction in water depth, between 1 and 3 meters, over a vast portion of the village compared to the previous version for the 20m DEM, while it is more balanced (reduction and increase in water depth in different portions of the village) for the 10m DEM. This highlights a strong interaction between the model physics and the topographic details, where the updated code produces a less severe inundation when run on a high-resolution DEM. However, as already mentioned in the previous section,



620 the effect of the use of different code versions is lower than the effect derived from the use of different DEMs, especially with respect to the inundated area.

Although the comparison between simulations performed using the 10 m and 20 m DEMs highlights significant differences in inundation patterns, these differences should not be interpreted solely in terms of grid resolution. Rather, they reflect a combination of factors related to data accuracy, data preprocessing, and the characteristic spatial scales of the physical processes involved. For the bathymetric domain, the new topobathymetry can be considered more accurate. The bathymetric data are more recent and originate from surveys with a much higher native resolution, allowing for a more reliable representation of near-shore morphology and, consequently, a more accurate simulation of tsunami wave propagation in the marine environment. For the subaerial domain, the interpretation is more complex. While the new topographic dataset is also more recent, it presents some intrinsic limitations. In particular, the DEM is not filtered for vegetation, and tall trees are therefore retained in the elevation model. As a consequence, these elements act as obstacles to tsunami propagation with dimensions comparable to the tree canopy, whereas the actual physical obstacle (the trunk) would have a much smaller impact. This effect is related to the lack of vegetation filtering in the source data rather than to the DEM resolution itself. In addition, the 10 m resolution represents an intermediate scale that is sufficient to partially resolve buildings, which may locally act as barriers to flow, but insufficient to properly represent narrow streets and alleys that characterize the built environment of Stromboli village. This combination may locally restrict flow propagation and result in inundation patterns that are influenced by partially resolved urban features. Conversely, the 20 m DEM introduces a stronger smoothing of small-scale features, reducing the influence of individual buildings and resulting in a more conservative representation of inundation extent over urban areas. For this reason, despite its coarser resolution, the 20 m DEM may provide a more conservative hazard assessment on land. Overall, it is therefore difficult to identify a single optimal DEM for tsunami hazard modelling at Stromboli. The two datasets present complementary advantages and limitations: the higher-resolution DEM offers a more accurate representation of marine wave propagation, while the coarser DEM may yield more conservative and stable inundation estimates on land. Presenting results obtained with both datasets allows these sources of epistemic uncertainty to be explicitly explored and communicated. Similarly, the choice of the landslide volume range involves a trade-off between completeness and methodological assumptions. The analysis including larger volumes ($\geq 1 \times 10^6 \text{ m}^3$, incorporating $40 \times 10^6 \text{ m}^3$ scenarios) provides a more comprehensive and conservative assessment of the hazard intensity, as it includes (although with limitations) all the scales of TLs identified by the four volume ranges defined in the elicitation. However, this required an assumption to handle the unbounded nature of the largest volume class elicited ($> 30 \times 10^6 \text{ m}^3$), for which we assigned the entire probability to the $40 \times 10^6 \text{ m}^3$ scenarios. While this approach captures the impact of high-consequence events, the choice of a single representative volume is an acknowledged simplification.

650 **4.2 Hazard assessment in critical areas of Stromboli village**

The primary and most critical finding of this work is the quantification of a high probability of tsunami inundation for the inhabited coastal areas of Stromboli over the next 50 years. The probabilistic maps show that significant inundation is not a



remote possibility but relatively likely. In particular, the 95th percentile maps - representing a severe but plausible “1-in-20” outcome from the range of expert uncertainty - indicate that widespread inundation by at least 0.5 m of water is likely. The hazard curves for critical sites reinforce this conclusion, showing non-negligible probabilities of exceeding damaging water depths. These results provide a first quantitative basis for civil protection authorities and stakeholders to inform risk mitigation strategies, emergency planning, and public awareness campaigns.

The remarkable stability observed when water depth threshold increases from 0.1 m to 1.0 m strongly suggests that the maximum inland penetration of the tsunami is dominated by the local topography rather than the specific height of the incoming wave. For the majority of the tsunamigenic scenarios, the waves likely possess sufficient energy to travel across the flat coastal plain until they are stopped by an abrupt change in slope at the edge of the village. The final inundation limit is therefore primarily a function of the terrain morphology, which acts as a natural barrier.

This finding has a critical implication for hazard assessment at Stromboli: in the vulnerable coastal areas, there is not a gradual relationship between wave height and inundation extent. Instead, once a minimal inundation threshold is surpassed, the flow is likely to occupy the entire susceptible low-lying area. This means that even scenarios producing waves of apparently moderate height (e.g., just over 1 m at the coast) can lead to a widespread and significant inundation across the village waterfront. Consequently, the entire low-lying coastal plain should be considered exposed to inundation, regardless of the specific tsunami scenario.

With respect to site-specific analysis, some comparison could be done with respect to sites where we developed hazard curves and the effect of the 2002 tsunami described in Bertagnini et al. (2003) and Tinti et al. (2006a). The site of “Spiaggia Lunga” (point 1 in Figure 1) is the area where the highest runup of all the 2002 event was measured (10.9 m; Tinti et al., 2006a). Despite the large uncertainty expressed by the 5th-95th percentile range, our hazard estimates indicate a probability of equalling or exceeding 0.5 m in the next 50 years that is consistently > 70% as median probability (depending on the database/volume range chosen; see Figs. S9-S12 from Supporting Information). Similarly, the “Centrale ENEL” site (which was flooded during the 2002 tsunami; Tinti et al., 2006a) shows probabilities for the same threshold consistently > 60% as median probability (see Fig. 11), indicating a major hazard for this very sensitive site. The “Area di attesa Ficogrande” site (Figs. 1 and 12), as previously noted, is located outside the inundation area of the 2002 tsunami, over which the current Italian civil protection plan is based (Protezione Civile, 2015). For this site, we highlight the dual behaviour observed when considering maps obtained with the Databases A and B (Fig. 12). While in fact for the 10 m database the probability of inundation is zero, Database A the probability of equalling or exceeding 0.5 m in the next 50 years is > 5% or > 10% as median probability, indicating a non-negligible hazard also for this site (taking also into account the capability of a tsunami wave of 0.5 to drag away an adult).

Figures 13 and 14 have a double advantage. From one side it could offer a quick view useful to identify trend in hazard assessment and link them to morphological aspects of the coastline. For example, in Figure 13 the decrease in probability values to the east of “Area di attesa Ficogrande” can be interpreted as a sheltering effect caused by the orientation of the coastline relative to the incoming waves from the northwest. Along the same line, the significant drop in probability occurring



in the easternmost section ("Centrale ENEL" to "Molo Scari") indicates that this area becomes progressively more shielded from the main tsunami impact.

On the other hand, hazard profiles are useful in case one would like to evaluate the hazard along a line describing the maximum runup of a known event (i.e., the measured maximum runup of the 2002 event; Tinti et al., 2006a). In our case, choosing the 15-m isoline is conservative with respect to the maximum runup measured for the 2002 event (10.9 m) but helps in evaluating the hazard along critical limits, that in our case is beyond the safe zone area as defined by the current Italian civil protection plan.

4.3 Limits and future developments of the current approach

The approach and the results described in previous sections represent a first step toward a more quantitative tsunami hazard assessment for Stromboli village. The large uncertainty quantified in our results is indicative of the high sensitivity of the investigated area with respect to even small fluctuations in both the volume/location of landslide but also to the probabilities of different scenarios in the next 50-year period.

To summarize some considerations from the previous sections, we wish to add that the maps/curves produced, when considered individually, may present certain limitations, specifically:

- Less accurate topobathymetry for maps/curves produced using 20 m simulations. On one hand, the source bathymetric data is less accurate; on the other, at a 20 m resolution, the smoothing of the topography produces a much more uniform inundation model, lacking visible effects of obstacles at the scale of individual buildings.
- At a 10 m resolution, the inundation maps clearly show the local effects of buildings or small natural elements on wave propagation. However, an even higher resolution is likely requisite for an accurate description of these effects, in order to model the impact of alleys and streets between individual buildings.
- Concentration of probability for the volume interval $V > 30 \times 10^6 \text{ m}^3$ within a single scenario ($40 \times 10^6 \text{ m}^3$) for maps/curves produced with simulations at both 10 m and 20 m with volumes $\geq 1 \times 10^6 \text{ m}^3$.

For future developments, higher-resolution DEMs, more accurate reconstruction of landslide volumes of past events, or updated estimates of landslide frequency could significantly modify both the spatial extent and intensity of the hazard. Future work could focus on incorporating these improvements to refine hazard estimates and reduce epistemic uncertainty.

5 Conclusions

This work provides the first probabilistic tsunami hazard assessment study for landslides induced by volcanic activity at Stromboli volcano along the Sciara del Fuoco. By integrating probabilities derived from expert elicitation and numerical modelling of different landslide scenarios (mainly different volumes and initial landslide positions), we produced inundation maps, hazard curves and hazard profiles, explicitly quantifying the large uncertainties inherent in the process (through the representation of maps/curves/profiles corresponding to 5th/50th/95th percentile values). These maps/curves were produced



taking into consideration the temporal framework of the next 50 years, as derived from the expert elicitation. We also explored the sensitivity of the results to: i) different resolution of the DEMs used for numerical modelling (10 m and 20 m), ii) different model version, and iii) different landslide volume range. In this way, we therefore offer a transparent basis for hazard assessment and mitigation planning. The sensitivity analysis indicates that the impact of the use of different DEMs is more important (when considering the extent of the inundated area) with respect to the use of different model versions and different landslide volume ranges.

Key products include hazard maps (for four fixed water depth thresholds and for two fixed probability values), hazard curves for 6 sensitive sites along the coast of Stromboli. In addition, hazard profiles along the specific 15-m elevation isoline are derived from the corresponding hazard maps to explore the hazard at specific elevations. Important findings of this work indicate that, from a qualitative point of view, the 95th percentile maps indicate that widespread inundation by at least 0.5 m of water is likely. More quantitatively, water depths of ≥ 0.5 m have a median probability of $> 60\%$, regardless of the DEM chosen or the landslide volume range considered, for the main critical infrastructure of Stromboli Island (i.e. the local power plant). In addition, for one of the most touristic beaches of the island (“Spiaggia Lunga”), in the next 50 years the median probability of the same water depth threshold is similarly $> 70\%$. Inspection of hazard profiles along specific isolines, indicates that for the 15-m elevation isoline there is still a considerable hazard that this zone could be impacted by tsunami waves ≥ 0.5 m. These hazard products may support coastal planning at Stromboli for volcano-generated tsunamis, including evacuation mapping for responses to alerts issued by the local tsunami warning system (Ripepe and Lacanna, 2024; Schindel  et al., 2024; UNESCO/IOC, 2024).

To conclude, it is important to recognize that PTHA is an evolving process. These maps and curves represent the current state of knowledge and should be considered a living product, subject to future updates as new data become available, numerical models improve, and our understanding of the underlying physical processes is refined.

Code and data availability

The simulations used to create hazard maps and curves are freely downloadable from de’ Michieli Vitturi (2026a-b) databases. The simulations presented in this study were carried out using the Multilayer-HySEA code. The source code is publicly available at the GitHub repository: <https://github.com/edanya-uma/Multilayer-HySEA>.

Author contributions

MdMV.: conceptualization, resources, data curation, investigation, visualization, software, methodology, supervision, project administration, methodology, writing – original draft, writing – review & editing, project administration; AT: conceptualization, resources, data curation, investigation, visualization, software, methodology, writing – original draft,

writing – review & editing; AB: conceptualization, resources, data curation, formal analysis, investigation, visualization, methodology, writing – review & editing; JFRG: resources, data curation, visualization, methodology, writing – review & editing; MC, TEO, AN, MT: conceptualization, resources, data curation, visualization, methodology, writing -review & editing; SL: methodology, writing – review & editing, project administration; JM, MJC, CE, SO, JMGV: software, writing – review & editing.

Competing interests

The authors declare no competing interests.

Financial support

This research has been supported by “Convenzione Attuativa per il potenziamento delle attività di servizio, Task 2.2” in the framework of “Accordo Quadro DPC-INGV 2022-2025”.

Acknowledgements

The contribution and support of ideas of Eugenio Privitera and Mauro Coltelli (INGV coordinators of the DPC-INGV agreement) and of many colleagues participating in the project are acknowledged. In particular, we wish to thank Massimiliano Favalli, Alessandro Fornaciai, Mauro Coltelli, Danilo Cavallaro and Marina Bisson for providing the topo-bathymetric data used to perform the simulations. We also thank Laura Sandri, Finn Løvholt, Stephan Grilli, Anne LeFriant and Bill Fry for useful comments and suggestions provided within the “Convenzione Attuativa per il potenziamento delle attività di servizio, Task 2.2”. The manuscript does not necessarily represent official views and policies of the Dipartimento della Protezione Civile.

References

Abadie, S., Aguirre-Ayerbe, I., Aniel-Quiroga, I., Babeyko, A., Baiguera, M., Basili, R., Belliazzi, S., Grezio, A., Johnson, K., Murphy, S., Paris, R., Rafliana, I., De Risi, R., Rossetto, T., Selva, J., Taroni, M., Del Zoppo, M., Armigliato, A., Bures, V., Cech, P., Cecioni, C., Christodoulides, P., Davies, G., Dias, F., Bayraktar, H. B., González, M., Gritsevich, M., Guillas, S., Harbitz, C. B., Kânoğlu, U., Macías, J., Papadopoulos, G. A., Polet, J., Romano, F., Salamon, A., Scala, A., Stepinac, M., Tappin, D. R., Thio, H. K., Tonini, R., Triantafyllou, I., Ulrich, T., Varini, E., Volpe, M., Vyhmeister, E., Behrens, J., Løvholt, F., Jalayer, F., Lorito, S., Salgado-Gálvez, M. A., Sørensen, M.: Probabilistic tsunami hazard and risk analysis: A review of research gaps. *Frontiers in Earth Science*, 9, 628772, doi: 10.3389/feart.2021.628772, 2021.

Aspinall, W. P.: A route to more tractable expert advice. *Nature* 463, 294–295, doi: 10.1038/463294a, 2010.

775

Aspinall, W. P.: Structured elicitation of expert judgement for probabilistic hazard and risk assessment in volcanic eruptions. In: Mader HM, Coles SG, Connor CB, Connor LJ (eds) *Statistics in Volcanology*. Geological Society of London, 15-30, doi: 10.1144/IAVCEI001.2, 2006.

780

Aspinall, W. P., Cooke, R.: Expert elicitation and judgement. In *Risk and uncertainty assessment in natural hazards*, Cambridge University Press, 234-274, 2013.

Barberi F., Rosi M., and Sodi A.: Volcanic Hazard Assessment at Stromboli Based on Review of Historical Data. *Acta Vulcanol.*, 3, 173–187, 1993.

785

Basili, R., Brizuela, B., Herrero, A., Iqbal, S., Lorito, S., Maesano, F.E., Murphy, S., Perfetti, P., Romano, F., Scala, A., Selva, J., Taroni, M., Thio, H.K., Tiberti, M.M., Tonini, R., Volpe, M., Glimsdal, S., Harbitz, C.B., Løvholt, F., Baptista, M.A., Carrilho, F., Matias, L.M., Omira, R., Babeyko, A., Hoechner, A., Gurbuz, M., Pekcan, O., Yalçiner, A., Canals, M., Lastras, G., Agalos, A., Papadopoulos, G., Triantafyllou, I., Benchekroun, S., Agrebi Jaouadi, H., Attafi, K., Ben Abdallah, S., Bouallegue, A., Hamdi, H., Oueslati, F.: NEAM Tsunami Hazard Model 2018 (NEAMTHM18): online data of the Probabilistic Tsunami Hazard Model for the NEAM Region from the TSUMAPS-NEAM project. Istituto Nazionale di Geofisica e Vulcanologia (INGV), doi: 10.13127/tsunami/neamthm18, 2018.

790

Basili R., Brizuela B., Herrero A., Iqbal S., Lorito S., Maesano F.E., Murphy S., Perfetti P., Romano F., Scala A., Selva J., Taroni M., Thio H.K., Tiberti M.M., Tonini R., Volpe M., Glimsdal S., Harbitz C.B., Løvholt F., Baptista M.A., Carrilho F., Matias L.M., Omira R., Babeyko A., Hoechner A., Gurbuz M., Pekcan O., Yalçiner A., Canals M., Lastras G., Agalos A., Papadopoulos G., Triantafyllou I., Benchekroun S., Agrebi Jaouadi K., Ben Abdallah S., Bouallegue A., Hamdi H., Oueslati F., Amato A., Armigliato A., Behrens J., Davies G., Di Bucci D., Dolce M., Geist E., Gonzalez Vida J.M., González M., Macías Sánchez J., Meletti C., Ozer Sozdinler C., Pagani M., Parsons T., Polet J., Power W., Sørensen M.B, Zaytsev A.: The making of the NEAM Tsunami Hazard Model 2018 (NEAMTHM18). *Front. Earth Sci.*, doi: 10.3389/feart.2020.616594, 2021.

800

Behrens, J., Løvholt, F., Jalayer, F., Lorito, S., Salgado-Gálvez, M. A., Sørensen, M., Abadie, S., Aguirre-Ayerbe, I., Aniel-Quiroga, I., Babeyko, A., Baiguera, M., Basili, R., Belliazzi, S., Grezio, A., Johnson, K., Murphy, S., Paris, R., Rafliana, I., De Risi, R., Rossetto, T., Selva, J., Taroni, M., Del Zoppo, M., Armigliato, A., Bureš, V., Cech, P., Cecioni, C., Christodoulides, P., Davies, G., Dias, F., Başak Bayraktar, H., González, M., Gritsevich, M., Guillas, S., Harbitz, C. B., Kânoğlu, U., Macías, J., Papadopoulos, G. A., Polet, J., Romano, F., Salamon, A., Scala, A., Stepinac, M., Tappin, D. R., Kie

805



Thio, H., Tonini, R., Triantafyllou, I., Ulrich, T., Varini, E., Volpe, M., & Vyhmeister, E.: Probabilistic tsunami hazard and risk analysis: A review of research gaps. *Frontiers in Earth Science*, 9, 628772, doi: 10.3389/feart.2021.628772, 2021.

810 Bertagnini, A., Papale, P., Santi, P.: Osservazioni e misure relative all'onda di maremoto del 30 dicembre 2002, effettuate lungo il paese di Stromboli dalla località Piscità al centro GNV eliporto PC. GNV Technical report, 4 pp., <https://gnv.ingv.it/pubblicazioni/Stima%20H%20massima%20Tsunami%20dic%202002.pdf>, 2003.

815 Bevilacqua, A.: Doubly stochastic models for volcanic hazard assessment at Campi Flegrei caldera, 227 pp., Birkhäuser/Springer, Pisa, doi: 10.1007/978-88-7642-577-6, 2016.

820 Bevilacqua, A., Isaia, R., Neri, A., Vitale, S., Aspinall, W. P., Bisson, M., Flandoli, F., Baxter, P. J., Bertagnini, A., Esposti Ongaro, T., Iannuzzi, E., Pistoiesi, M., Rosi, M.: Quantifying volcanic hazard at Campi Flegrei caldera (Italy) with uncertainty assessment: 1. Vent opening maps. *Journal of Geophysical Research: Solid Earth* 120(4), 2309–2329, doi: 10.1002/2014jb011775, 2015.

825 Bevilacqua, A., de' Michieli Vitturi, M., Tadini, A., Neri, A., Aspinall, W. P., and Sparks, R. S. J.: The Kolumbo Volcanic Field, Greece: expert elicitation findings supporting volcanic hazard and risk assessment. *Bull. Volcanol.*, 87, 41, doi:10.1007/s00445-025-01822-3, 2025.

Bisson, M., Gianardi, R., Civico, R., Madonia, P., Ricci, T., Spinetti, C.: Stromboli DSM 2023. INGV Ufficio Dati, doi: 10.13127/stromboli/airborne-lidar-2023, 2025.

830 Bonilauri, E. M., Harris, A. J., Morin, J., Ripepe, M., Mangione, D., Lacanna, G., Ciolli, S., Cusolito, M., and Deguy, P.: Tsunami evacuation times and routes to safe zones: a GIS-based approach to tsunami evacuation planning on the island of Stromboli, Italy. *J. Appl. Volcanol.*, 10(1), 4, doi:10.1186/s13617-021-00104-9, 2021.

835 Brunetti, M. T., Guzzetti, F., and Rossi, M.: Probability distributions of landslide volumes. *Nonlinear Process. Geophys.*, 16(2), 179–188, doi:10.5194/npg-16-179-2009, 2009.

840 Cerminara, M., Esposti Ongaro, T., de' Michieli Vitturi, M., Tadini, A., Trolese, M., Fornaciai, A., Nannipieri, L., Rodriguez Galvez, J. F.: Simulated scenarios of volcanic mass movements and associated tsunamis at Stromboli (Aeolian archipelago, Tyrrhenian Sea, Italy). version 1 [Data set]. Istituto Nazionale di Geofisica e Vulcanologia (INGV). Doi: 10.13127/stromboli/sciara_del_fuoco_tsunami, 2024.



Chiocci, F. L., Ridente, D.: Regional-scale seafloor mapping and geohazard assessment. The experience from the Italian project MaGIC (Marine Geohazards along the Italian Coasts). *Marine Geophysical Research* 32(1–2), 13–23, doi: 10.1007/s11001-011-9120-6, 2011.

845 Colson, A. R., Cooke, R. M.: Expert elicitation: using the classical model to validate experts' judgments. *Review of Environmental Economics and Policy*, doi: 10.1093/reep/rex022, 2018.

Constantinescu, R., González-Zuccolotto, K., Ferrés, D., Sieron, K., Siebe, C., Connor, C., Capra, L., and Tonini, R.: Probabilistic volcanic hazard assessment at an active but under-monitored volcano: Ceboruco, Mexico. *Journal of Applied*
850 *Volcanology*, 11(1), 11, doi: 10.1186/s13617-022-00119-w, 2022.

Cooke, R. M.: *Experts in uncertainty: opinion and subjective probability in science*, 1991.

Cordie, L., Selva, J., Bernardi, F., Tonini, R., Romano, F., Volpe, M., and Lorito, S.: Dynamic management of uncertainty in
855 rapid tsunami forecasting. *Communications Earth & Environment*, 6(1), 637, doi: 10.1038/s43247-025-02586-6, 2025.

Dalrymple, R.A., Grilli, S.T., and Kirby, J.T.: Tsunamis and challenges for accurate modeling. *Oceanography* 19(1):142–151,
[doi: 10.5670/oceanog.2006.97](https://doi.org/10.5670/oceanog.2006.97), 2006

860 de' Michieli Vitturi, M., Bevilacqua, A., Tadini, A., and Neri, A.: ELICIPY 1.0: a Python online tool for expert elicitation. *SoftwareX*, 25, 101641, doi: 10.1016/j.softx.2024.101641, 2024.

de' Michieli Vitturi M., Tadini A., Bevilacqua A., Rodríguez Gálvez J. F., Cerminara M., Esposti Ongaro T., Neri A., Trolese
865 M., Macías J., Castro M. J., Escalante C., Ortega S., and González-Vida J. M.: Simulated scenarios of volcanic mass
movements and associated tsunamis at Stromboli (Aeolian archipelago, Tyrrhenian sea, Italy) - version 2, simulations with
20-m resolution topo-bathymetry. [Dataset]. INGV Ufficio Dati, <https://www.pi.ingv.it/banche-dati/scenarios-of-volcanic-mass-movements-associated-tsunamis-at-stromboli-20-m-topo-bathymetry/>, 2026a.

870 de' Michieli Vitturi M., Tadini A., Bevilacqua A., Rodríguez Gálvez J. F., Cerminara M., Esposti Ongaro T., Neri A., Trolese
M., Macías J., Castro M. J., Escalante C., Ortega S., and González-Vida J. M.: Simulated scenarios of volcanic mass
movements and associated tsunamis at Stromboli (Aeolian archipelago, Tyrrhenian sea, Italy) - version 2, simulations with
10-m resolution topo-bathymetry. [Dataset]. INGV Ufficio Dati, <https://www.pi.ingv.it/banche-dati/scenarios-of-volcanic-mass-movements-and-associated-tsunamis-at-stromboli-10-m-topo-bathymetry/>, 2026b.



875 Di Traglia, F., Calvari, S., D’Auria, L., Nolesini, T., Bonaccorso, A., Fornaciai, A., Esposito, A., Cristaldi, A., Favalli, M.,
Casagli, N.: The 2014 Effusive Eruption at Stromboli: New Insights from In Situ and Remote-Sensing Measurements. *Remote
Sens.* 10, 2035, doi: 10.3390/rs10122035, 2018.

880 Di Traglia, F., Fornaciai, A., Casalbore, D., Favalli, M., Manzella, I., Romagnoli, C., Chiocci, F. L., Cole, P., Nolesini, T.,
Casagli, N.: Subaerial-submarine morphological changes at Stromboli volcano (Italy) induced by the 2019–2020 eruptive
activity. *Geomorphology*, 400, 108093, doi: 10.1016/j.geomorph.2021.108093, 2022.

885 Escalante, C., de Luna, T. M., Castro, M. J.: Non-hydrostatic pressure shallow flows: GPU implementation using finite volume
and finite difference scheme. *Applied Mathematics and Computation*, 338, 631–659, doi: 10.1016/j.amc.2018.06.035, 2018.

Escalante, C., Fernández-Nieto, E. D., de Luna, T. M., Castro, M. J.: An efficient two-layer non-hydrostatic approach for
dispersive water waves. *Journal of Scientific Computing*, 79, 273–320, doi: 10.1007/s10915-018-0849-9, 2019.

890 Esposti Ongaro, T., de’Michieli Vitturi, M., Cerminara, M., Fornaciai, A., Nannipieri, L., Favalli, M., Calusi, B., Macías, J.,
Castro, M. J., Ortega, S., González-Vida, J. M., Escalante, C.: Modeling tsunamis generated by submarine landslides at
Stromboli Volcano (Aeolian Islands, Italy): A numerical benchmark study. *Frontiers in Earth Science*, 9, 628652, doi:
10.3389/feart.2021.628652, 2021.

895 Esposti Ongaro, T., Cerminara, M., de’Michieli Vitturi, M., Tadini, A., Trolese, M., Fornaciai, A., Nannipieri, L., Calusi, B.,
Macías, J., Castro, M. J., Escalante, C., Acosta, S. O., González-Vida, J. M., Rodríguez Galvez, J. F.: Modeling and numerical
simulation of volcanic mass movements and associated tsunamis at Stromboli (Aeolian archipelago, Tyrrhenian sea, Italy).
Frontiers in Earth Science, 13, 1548961, doi: 10.3389/feart.2025.1548961, 2025.

900 Fernández-Nieto, E. D., Bouchut, F., Bresch, D., Castro Díaz, M. J., Mangeney, A.: A new Savage–Hutter type model for
submarine avalanches and generated tsunamis. *Journal of Computational Physics*, 227, 7720–7754, doi:
10.1016/j.jcp.2008.04.039, 2008.

905 Fernández-Nieto, E. D., Garres-Díaz, J., Mangeney, A., Narbona-Reina, G.: 2D granular flows with the $\mu(I)$ rheology and side
walls friction: A well-balanced multilayer discretization. *Journal of Computational Physics*, 356, 192–219, doi:
10.1016/j.jcp.2017.11.038, 2018.

Fornaciai, A., Favalli, M., Nannipieri, L.: Numerical simulation of the tsunamis generated by the Sciara del Fuoco landslides
(Stromboli Island, Italy). *Scientific reports*, 9(1), 18542, doi: 10.1038/s41598-019-54949-7, 2019.



- 910 Fukutani, Y., Moriguchi, S., Terada, K., and Otake, Y.: Time-dependent probabilistic tsunami inundation assessment using mode decomposition to assess uncertainty for an earthquake scenario. *Journal of Geophysical Research: Oceans*, 126(7), e2021JC017250, doi: 10.1029/2021JC017250, 2021.
- Gibbons, S. J., Lorito, S., Macías, J., Løvholt, F., Selva, J., Volpe, M., Sánchez-Linares, C., Babeyko, A., Brizuela, B., Cirella, 915 A., Castro, M. J., de la Asunción, M., Lanucara, P., Glimsdal, S., Lorenzino, M. C., Nazaria, M., Pizzimenti, L., Romano, F., Scala, A., Tonini, R., Manuel González-Vida, J., and Vöge, M.: Probabilistic Tsunami Hazard Analysis: High Performance Computing for Massive Scale Inundation Simulations. *Front. Earth Sci.*, 8:591549, doi: 10.3389/feart.2020.591549, 2020.
- Glimsdal, S., Løvholt, F., Harbitz, C. B., Romano, F., Lorito, S., Orefice, S., Brizuela, B., Selva, J., Hoechner, A., Volpe, M., 920 Babeyko, A., Tonini, R., Wronna, M., and Omira, R.: A new approximate method for quantifying tsunami maximum inundation height probability. *Pure and Applied Geophysics*, 176(7), 3227-3246, doi: 10.1007/s00024-019-02091-w, 2019.
- Grezio, A., Babeyko, A., Baptista, M. A., Behrens, J., Costa, A., Davies, G., Geist, E. L., Glimsdal, S., González, F. I., Griffin, J., Harbitz, C. B., LeVeque, R. J., Lorito, S., Løvholt, F., Omira, R., Mueller, C., Paris, R., Parsons, T., Polet, J., Power, W., 925 Selva, J., Sørensen M. B., Thio, H. K.: Probabilistic tsunami hazard analysis: multiple sources and global applications. *Reviews of Geophysics*, 55(4), 1158-1198, doi: 10.1002/2017RG000579, 2017.
- Griffin, J., Latief, H., Kongko, W., Harig, S., Horspool, N., Hanung, R., Rojali, A., Maher, N, Fuchs, A., Hossen, J., Supryati, U., Dewanto, S. E., Rakowsky, N., and Cummins, P.: An evaluation of onshore digital elevation models for modeling tsunami 930 inundation zones. *Front. Earth Sci.* 3:32. doi: 10.3389/feart.2015.00032, 2015.
- Horspool, N., Pranantyo, I., Griffin, J., Latief, H., Natawidjaja, D. H., Kongko, W., Cipta, A., Bustaman, B., Anugrah, S. D., Thio, H. K.: A probabilistic tsunami hazard assessment for Indonesia. *Natural Hazards and Earth System Sciences*, 14(11), 3105-3122, doi: 10.5194/nhess-14-3105-2014, 2014. 935
- Kaiser, G., Scheele, L., Kortenhaus, A., Løvholt, F., Römer, H., and Leschka, S.: The influence of land cover roughness on the results of high resolution tsunami inundation modeling. *Nat. Hazards Earth Syst. Sci.* 11, 2521–2540. doi: 10.5194/nhess-11-2521-2011, 2011.
- 940 Kurisu, A., Suga, H., Prochazka, Z., Suzuki, K., Oguri, K., and Inoue, T.: Potential technique for improving the survival of victims of tsunamis. *PLoS one*, 13(5), e0197498, doi: 10.1371/journal.pone.0197498, 2018.



Jaccard, P.: Étude comparative de la distribution florale dans une portion des Alpes et des Jura. *Bull Soc Vaudoise Sci Nat*, 37, 547-579, 1901.

945

Løvholt, F., Glimsdal, S., and Harbitz, C. B.: On the landslide tsunami uncertainty and hazard. *Landslides*, 17(10), 2301-2315, doi: 10.1007/s10346-020-01429-z, 2020.

950

Lorito, S., Selva, J., Basili, R., Romano, F., Tiberti, M. M., and Piatanesi, A.: Probabilistic hazard for seismically induced tsunamis: accuracy and feasibility of inundation maps. *Geophysical Journal International*, 200(1), 574-588, doi: 10.1093/gji/ggu408, 2015.

955

Lorito, S., Behrens, J., Løvholt, F., Rossetto, T., and Selva, J.: From tsunami science to hazard and risk assessment: Methods and models. *Frontiers in Earth Science*, 9, 764922, doi: 10.3389/feart.2021.764922, 2021.

Macías, J., Escalante, C., Castro, M. J.: Multilayer-HySEA model validation for landslide generated tsunamis – Part 1: Rigid slides. *Natural Hazards and Earth System Sciences*, 21, 775–789, doi: 10.5194/nhess-21-775-2021, 2021a.

960

Macías J, Escalante C, Castro MJ: Multilayer-HySEA model validation for landslide generated tsunamis – Part 2: Granular slides. *Natural Hazards and Earth System Sciences*, 21, 791–805, doi: 10.5194/nhess-21-791-2021, 2021b.

MASE: DTM LiDAR con risoluzione a terra 1 metro - Regione Sicilia, Geoportale Nazionale, Ministero dell’Ambiente e della Sicurezza Energetica, <http://www.pcn.minambiente.it/>, 2013.

965

Neri, A., Aspinall, W. P., Cioni, R., Bertagnini, A., Baxter, P. J., Zuccaro, G., Andronico, D., Barsotti, S., Cole, P.D., Esposti Ongaro, T., Hincks, T.K., Macedonio, G., Papale, P., Rosi, M., Santacroce, R., & Woo, G.: Developing an event tree for probabilistic hazard and risk assessment at Vesuvius. *J. Volcanol. Geotherm. Res.*, 178(3), 397-415, doi: 10.1016/j.jvolgeores.2008.05.014, 2008.

970

Neri, A., Bevilacqua, A., Esposti Ongaro, T., Isaia, R., Aspinall, W. P., Bisson, M., Flandoli, F., Baxter, P. J., Bertagnini, A., Iannuzzi, E., Orsucci, S., Pistolesi, M., Rosi, M., and Vitale, S.: Quantifying volcanic hazard at Campi Flegrei caldera (Italy) with uncertainty assessment: 2. Pyroclastic density current invasion maps. *Journal of Geophysical Research: Solid Earth*, 120(4), 2330-2349, doi: 10.1002/2014JB011776, 2015.



975 Paris, R., Ulvrová, M., Selva, J., Brizuela, B., Costa, A., Grezio, A., Lorito, S., Tonini, R.: Probabilistic hazard analysis for tsunamis generated by subaqueous volcanic explosions in the Campi Flegrei caldera, Italy. *Journal of Volcanology and Geothermal Research*, 379, 106-116, doi: 10.1016/j.jvolgeores.2019.05.010, 2019.

Protezione Civile: <https://rischi.protezionecivile.gov.it/en/volcanic/volcanoes-italy/stromboli/emergency-planning/>, last
980 access 15 March 2026, 2015.

Protezione Civile: <https://www.protezionecivile.gov.it/en/normativa/decreto-legislativo-n-1-del-2-gennaio-2018--codice-della-protezione-civile/>, last access 15 March 2026, 2018a.

985 Protezione Civile: <https://rischi.protezionecivile.gov.it/static/0d78a388122669d46d9a7df0a09cc562/indicazioni-siam-senza-allegati.pdf>, last access 15 March 2026, 2018b.

Quigley, J., Colson, A., Aspinall, W., Cooke, R.M.: Elicitation in the Classical Model. In: Dias, L., Morton, A., Quigley, J. (eds) *Elicitation. International Series in Operations Research & Management Science*, vol 261. Springer, Cham, doi:
990 10.1007/978-3-319-65052-4_2, 2018.

Ramos, M., Aránguiz, R., and Bull, M. T.: Tsunami inundation limit based on probabilistic analysis of runup and inundation distance. *Natural Hazards*, 121(3), 2719-2745, doi: 10.1007/s11069-024-06916-3, 2025.

995 Ripepe, M., and Lacanna, G.: Volcano generated tsunamis recorded in the near source. *Nat. Commun.*, 15(1), 1802, doi:10.1038/s41467-024-45937-1, 2024.

Scala, A., Lorito, S., Escalante Sánchez, C., Romano, F., Festa, G., Abbate, A., Bayraktar, H. B., Castro, M. J., Macías, J., and Gonzalez-Vida, J. M.: Assessing the optimal tsunami inundation modeling strategy for large earthquakes in subduction zones.
1000 *Journal of Geophysical Research: Oceans*, 129(9), e2024JC020941, doi: 10.1029/2024JC020941, 2024.

Schindelé, F., Kong, L., Lane, E. M., Paris, R., Ripepe, M., Titov, V., and Bailey, R.: A review of tsunamis generated by volcanoes (TGV) source mechanism, modelling, monitoring and warning systems. *Pure Appl. Geophys.*, 181(6), 1745–1792, doi:10.1007/s00024-024-03515-y, 2024.

1005 Selva, J., Lorito, S., Volpe, M., Romano, F., Tonini, R., Perfetti, P., Bernardi, F., Taroni, M., Scala, A., Babeyko, A., Løvholt, F., Gibbons, S. J., Macías, J., Castro, M. J., González-Vida, J. M., Sánchez-Linares, C., Bayraktar, H. B., Basili, R., Maesano,



F. E., Tiberti, M. M., Mele, F., Piatanesi, A., Amato, A.: Probabilistic tsunami forecasting for early warning. *Nature communications*, 12(1), 5677, doi: 10.1038/s41467-021-25815-w, 2021.

1010

Song, J., and Goda, K.: Influence of elevation data resolution on tsunami loss estimation and insurance rate-making. *Frontiers in Earth Science*, 7, 246, doi: 10.3389/feart.2019.00246, 2019.

1015

Tadini, A., Bevilacqua, A., Neri, A., Cioni, R., Aspinall, W. P., Bisson, M., Isaia, R., Mazzarini, F., Valentine, G. A., Vitale, S., Baxter, P. J., Bertagnini, A., Cerminara, M., de Michieli Vitturi, M., di Roberto, A., Engwell, S., Esposti Ongaro, T., Flandoli, F., Pistolesi, M.: Assessing future vent opening locations at the Somma-Vesuvio volcanic complex: 2. Probability Maps of the caldera for a future Plinian/sub-Plinian Event with uncertainty quantification. *Journal of Geophysical Research: Solid Earth* 122(6), 4357–4376, doi: 10.1002/2016jb013860, 2017.

1020

Tadini, A., Harris, A., Morin, J., Bevilacqua, A., Peltier, A., Aspinall, W., Ciolli, S., Bachèlery, P., Bernard, B., Biren, J., Brum da Silveira, A., Cayol, V., Chevrel, O., Coppola, D., Dietterich, H., Donovan, A., Dorado, O., Drenne, S., Dupéré, O., Gurioli, L., Kolzenburg, S., Komorowski, J.-C., Labazuy, P., Mangione, D., Mannini, S., Martel-Asselin, F., Médard, E., Pailot-Bonnétat, S., Rafflin, V., Ramsey, M., Richter, N., Vallejo, S., Villeneuve, N., Zafrilla, S.: Structured elicitation of expert judgement in real-time eruption scenarios: an exercise for Piton de la Fournaise volcano, La Réunion island. *Volcanica*, 5(1), 105–131, doi: 10.30909/vol.05.01.105131, 2022.

1025

Tadini, A., Bevilacqua, A., de' Michieli Vitturi, M., Bonilauri, E., Harris, A., Cerminara, M., Esposti Ongaro, T., Neri, A., Paris, R., Pistolesi, M., Trolese, M., Rodriguez Gálvez, J. F., Andronico, D., Bertagnini, A., Calvari, S., Casalbore, D., Cassidy, M., Civico, R., Del Bello, E., Di Roberto, A., Fornaciai, A., Grezio, A., Gurioli, L., Harbitz, C. B., Lacanna, G., Løvholt, F., Marani, M., Pompilio, M., Rosi, M., Sandri, L., Urgeles, R., Voloschina, M.: Probabilistic tsunami hazard assessment at Stromboli volcano: 1. Review of historical sources and expert elicitation findings. *Nat. Hazards Earth Syst. Sci.*, submitted.

1030

Tadini, A., Pardini, F., Bevilacqua, A., Bernard, B., Samaniego, P., de' Michieli Vitturi, M., Aravena, A., Hidalgo, S., Roche, O., Azzaoui, N., Neri, A., and Aguilar, J.: Probabilistic tephra fallout hazard maps for Sangay volcano, Ecuador. *Bulletin of Volcanology*, 87(2), 10, doi: 10.1007/s00445-025-01794-4, 2025.

1035

Tinti, S., Bortolucci, E., & Romagnoli, C.: Computer simulations of tsunamis due to sector collapse at Stromboli, Italy. *J. Volcanol. Geoth. Res.*, 96(1-2), 103-128, doi: 10.1016/S0377-0273(99)00138-9, 2000.

1040

Tinti, S., Armigliato, A., Manucci, A., Pagnoni, G., & Zaniboni, F.: Landslides and tsunamis of 30th December 2002 at Stromboli, Italy: numerical simulations. *Bollettino di Geofisica Teorica ed Applicata*, 46(2–3), 153-168, 2005.



1045 Tinti, S., Maramai, A., Armigliato, A., Graziani, L., Manucci, A., Pagnoni, G., and Zaniboni, F.: Observations of physical effects from tsunamis of December 30, 2002 at Stromboli volcano, southern Italy. *Bull. Volcanol.*, 68, 450–461, doi:10.1007/s00445-005-0021-x, 2006a.

Tinti, S., Pagnoni, G., Zaniboni, F.: The landslides and tsunamis of the 30th of December 2002 in Stromboli analysed through numerical simulations. *Bull. Volcanol.*, 68, 462–479, doi: 10.1007/s00445-005-0022-9, 2006b.

1050 Tonini, R., Di Manna, P., Lorito, S., Selva, J., Volpe, M., Romano, F., Basili, R., Brizuela, B., Castro, M. J., de la Asunción, M., Di Bucci, D., Dolce, M., Garcia, A., Gibbons, S. J., Glimsdal, S., González-Vida, J. M., Løvholt, F., Macías, J., Piatanesi, A., Pizzimenti, L., Sánchez-Linares, C., and Vittori, E.: Testing Tsunami Inundation Maps for Evacuation Planning in Italy. *Front. Earth Sci.* 9:628061, doi: 10.3389/feart.2021.628061, 2021.

1055 UNESCO/IOC: Monitoring and Warning for Tsunamis Generated by Volcanoes, Paris, UNESCO, IOC Technical Series No.183, 2024.

1060 Volpe, M., Lorito, S., Selva, J., Tonini, R., Romano, F., Brizuela, B.: From regional to local SPTHA: efficient computation of probabilistic tsunami inundation maps addressing near-field sources. *Natural Hazards and Earth System Sciences*, 19(3), 455–469, doi: 10.5194/nhess-19-455-2019, 2019.

Woessner, J., and Farahani, R. J.: Tsunami inundation hazard across Japan. *International journal of disaster risk reduction*, 49, 101654, doi: 10.1016/j.ijdr.2020.101654, 2020.